Master of Science Thesis: A friction study of densely grafted polymer brushes

Matthew Rigby
Department of Physics
McGill University

February 2014

A thesis submitted to McGill University in partial fulfilment of the requirements of the degree of M.Sc.

Abstract

This thesis outlines the development of a new method for friction force measurements using atomic force microscopy. It is compared to the standard friction force microscopy technique for verification. This new method is used to investigate the friction properties in the boundary lubrication regime of a novel polymer brush sample with a very high grafting density. It is found that there is no correlation between friction coefficient and the surrounding fluid's pH or salt concentration, and that the coefficient of friction is on the order of 0.1.

Résumé

La présente thèse aborde le développement d'une nouvelle méthode pour les mesures de friction à l'aide d'un microscope à force atomique. Elle est comparée à la méthode standard pour vérification. Cette nouvelle méthode est utilisée afin d'investiguer les propriétés dans le régime de la limite de lubrification d'un nouvel échantillon de brosse de polymères à très haute densité. Aucune corrélation n'a été trouvé entre le coefficient de friction et le pH ou la concentration de sel du fluide environnant. Le coefficient de friction mesuré est de l'ordre de 0.1.

Acknowledgements

Thanks to Peter for knowledge and guidance throughout my thesis. Thanks to Yoichi for helping me with any problem I ever had, and to all my labmates for engaging discussions and for encouragement. Thank you to all my family and friends who supported me throughout my thesis, especially towards the end when I really needed motivation.

Statement of Originality

The author, Matthew Rigby, claims the following aspects of the work contained herein constitute original scholarship and an advancement of knowledge:

- Development of a new method for friction force measurements using atomic force microscopy called friction force distance curve microscopy (FFDCM)
- Improvements of the method for gluing beads onto cantilevers.
- A method for the systematic subtraction of the Bioscope tracking lens error.
- Correction of photodiode non-linearities to linearise force distance curves.
- Kinetic friction measurements of PS-b-PAA polymer brushes in different salt concentrations and pH conditions.

Contents

List of Figures

List of Tables

1

Introduction

All mechanical systems transfer loads between components that move relative to one another, usually by rolling or sliding. [1] Friction is a resistance to this movement, converting the system's kinetic energy into heat. This energy loss can cause wear, a degradation of the material, and affects at least one of the surfaces involved. Given the destructive nature of wear, it is often the source of mechanical system failure. [2, 3]. Minimization of friction and wear is thus of central importance in any mechanical system, particularly in components with large power transfers, and where longevity is desired.

1.1 Introduction to Tribology

In 1966, for a government report in Britain, Peter Jost first popularized the term 'tribology', which includes the study of friction, wear and lubrication. [4] He reported that friction, wear and corrosion were costing the UK huge sums of money every year. [4] This prompted the government (and other countries) to open many national institutes for tribology research, and this research continues with vigor today.

Friction has been identified as a problem and efforts have been made to minimize it for thousands of years. [4] The first documented quantitative study was performed by Leonardo Da Vinci (1452-1519), but was left unpublished, so credit has gone mainly to Guillaume Amontons for his paper in 1699 for the first 2 laws of friction and to Charles-Augustin de Coulomb (1785) for the third. [4] They are now stated as follows:

1. The force of friction is directly proportional to the applied load.
2. The force of friction is independent of the apparent area of contact.

3. The force of kinetic friction is independent of the relative velocity between the contacting surfaces.

Using the first equation, we can obtain the coefficient of friction μ_k as the ratio of the friction force F_L over the normal force F_N:

$$\mu_k = \frac{F_L}{F_N} \tag{1.1}$$

1.1.1 Friction Theory

Amontons and Coulomb both postulated that the origin of friction was due to the physical interlocking of asperities, and was equal to the force needed to overcome these physical blockages. [4] Coulomb went further by adding a term due to adhesion to the right side of equation 1.1. [5] The problem was that friction had been shown to be independent of its area of contact, so this concept was ignored until Tomlinson revived it in 1929. Given some new knowledge of the microscopic nature of surfaces, he said that the force of friction arises from the energy needed to overcome adhesion and other forces fields that keep the materials together. [6] Both the normal and lateral forces would thus depend on the forces between interacting surfaces. [4,6,7] This thermodynamical view in terms of energy lost and gained is much more accurate than the purely mechanical view Amontons and Coulomb had. However, further microscopic details of the surface were needed to quantify these ideas.

In 1970, Bowden and Tabor showed importantly that contact between surfaces only occurs at asperities such that the ’real’ contact area A_{real} is orders of magnitude smaller than the apparent area. [8] They proposed a new equation for the lateral force:

$$F_L = \tau A_{real} \tag{1.2}$$

where τ is the shear strength and is a property of the material which resists lateral structural failure and the real contact area is given by: [4]

$$A_{real} = \frac{F_N}{\sigma_{yield}} \tag{1.3}$$

where σ_{yield} is the yield stress and depends on the resistance of both contact materials' asperities to deformation. We therefore obtain an expression for the coefficient of friction in terms of only material properties by plugging equations 1.3 and 1.2 into equation 1.1:

$$\mu_k = \frac{\tau}{\sigma_{yield}} \tag{1.4}$$

This description was extremely useful, but it is not consistent with Hertz' continuum model for the deformation of purely elastic spheres where $A \propto F_N^{\frac{2}{3}}$. [9] Moreover, the equation for contact area (equation 1.3) must be modified to include the contribution of adhesive forces when contact occurs on small scales (as in single asperity contact or in the case of an AFM tip) because the surface-to-bulk ratio increases significantly. [10]

Calculating the real contact area is done according to limiting cases of deformation. The Johnson-Kendall-Roberts (JKR) model describes the case where the contact area is maximized. This is where there is strong adhesion, at least one material is quite soft, and the tip is very large. [11] The other limiting case, where the contact area is minimized is described by the Derjarguin-Landau-Verwey (DLV) model. This is where there is weak adhesion, both materials are stiff and the tip is very sharp. [12] The more general Maugis-Dugdale(MD) model can describe intermediate contact areas where neither model for the limiting cases is sufficient. The model uses a transition parameter which depends on the reduced elastic modulus of the two materials and the work of adhesion between them. [13]

There are certain cases where the assumptions made for these models do not hold. They are for instance, by definition, continuum models even though the strain in the material has been shown to sometimes be discontinuous, and depend on the roughness of the surface. [14] They also assume that the surface will respond elastically, but in some cases, surfaces have been shown to have non-linear responses. [14]

1.1.2 Modern Friction Measurement Tools

Given the complexity of the interactions at the interface between materials, it is very hard to derive the laws of friction from first principles. [4, 15] For this reason, most analysis and theory have been developed empirically. The most popular current tools for investigating friction properties on the micro- and nano-scale are atomic force microscopy (AFM), the surface force apparatus (SFA), scanning tunnelling microscopy (STM) [16,17] and the Quartz crystal microbalance, [17,18] complemented by molecular dynamics simulations.

Since the inception of the atomic force microscope in 1986, [19] AFM has been used to measure lateral forces. [20] Some of the first lateral force experiments were performed by Mate et al. to observe atomic stick-slip behaviour. This supported Tomlinson's theory that the lateral force depends on the number of interacting molecules at the interface. [7,20] AFM has been an ideal tool for understanding the fundamental mechanisms behind friction and adhesion. This is because tips can probe single asperity contacts with contact areas on the order of $10nm^2$, while applying large pressures on the order of $1GPa$. [21] With the appropriate choice of cantilever and by varying the area of contact (eg. by gluing a bead underneath the cantilever), most desired force detection sensitivities in friction are possible. Using AFM, the Carpick-Ogletree-Salmeron (COS) transition parameter was developed which is an empirical approximation of the MD continuum model, such that the contact area or normal load can be fit as a function of the friction force. [10]

The surface force apparatus (SFA) was invented in the early 1970s, and has remained a very common technique for measuring friction. [22,23] It has vertical resolution on the order of 1 Å, and force detection on the order of 10nN. [9] However, it is limited when measuring very weak forces and imaging nanoscopic surface geometries. Although it is simpler to use than AFM (mainly due to a lengthy lateral calibration in AFM), SFA can only be used with mica (and vapors or solvents) because it requires molecularly thin and smooth surfaces. [23] The scanning tunnelling microscope (STM) was a precursor to the AFM, and so was used prior to the AFM for friction measurements. It is easier to obtain high resolution, but is limited in functionality as it can only measure electrically conducting surfaces. Quartz crystal microbalance has also been used in friction studies, but has generally been limited to high frequency friction measurements. [24]

Molecular dynamics (MD) simulations have progressed dramatically, now with capabilities to simulate both chemical and physical processes. [25,26] Of particular interest is the ability to follow heat dissipation from friction, and it's subsequent pathway. Advances in modelling and computing power have allowed the complex frictional problem to be visualized by the ability to include a multitude of interaction forces, as well as other complexities such as asymmetries, discrete effects and higher order non-linear effects. [26,27]

1.2 Lubrication

Friction is often not desired because of the material wear that accompanies it. In the case of adhesive and abrasive wear, the volume of material removed is directly proportional to the normal load (because it is directly related to the friction) and the sliding distance and inversely proportional to the hardness of the surface. [28] Minimizing the friction and thus the wear of a material can be achieved by altering the dynamics of their contact by introducing another substance between the contacting surfaces. This strategy can dramatically reduce the friction coefficient of the interacting surfaces, and is known as lubrication. [3]

Reynolds found that the thickness h_0 of the lubricating substance that separates the load bearing surfaces is directly proportional to the viscosity of the substance ν and the relative velocity of the surfaces v, and inversely proportional to the pressure applied on the surface P. This was crucial to the study of tribology because the friction coefficient is dependent on the thickness of the lubricant as shown in the Stribeck curve (1902) in figure 1.1. [3] The ratio (Λ) of the thickness of the lubricant h_{min} to the asperity heights for the contacting surfaces is what determines the friction regimes showed in the Stribeck Curve:

$$\Lambda = \frac{h_{min}}{\sqrt{R_{RMS1}^2 + R_{RMS2}^2}} \tag{1.5}$$

Where R_{RMS1} and R_{RMS2} are the root mean squared heights of the asperities for each of the contacting surfaces respectively.

Using this definition and the Stribeck curve, the three different friction regimes due to lubrication can be defined. The regimes are depicted in figure 1.1 by the curves A, A-B and B-C or B-D for hydrodynamic, mixed and boundary lubrication respectively. Hydrodynamic lubrication is the regime in which the film completely separates the interacting surfaces ($\Lambda > 5$), and friction is not due to the two surfaces interacting, but due to the viscosity of the fluid. [2,3,29] For Newtonian fluids (eg. water or oil), their is a direct dependence on viscosity of the film,

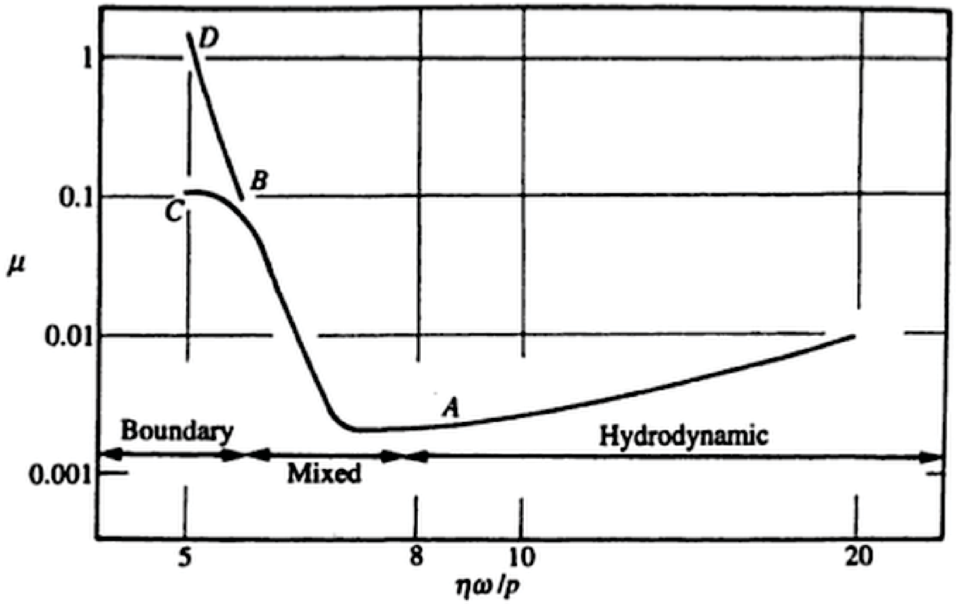

Figure 1.1: Characteristic Stribeck Curve from reference [3]. Shows the friction regimes due to lubrication and the dependence of the friction coefficient on the viscosity of the lubricant ν, the angular frequency ω (or equivalently the relative velocity v) of the involved surfaces and the pressure applied on the surface P.

with the friction coefficient increasing with fluid volume. [2,3,29] As the film size decreases such that $5 > \Lambda > 1$, the lubrication regime is said to be 'mixed' because the fluid supports the load, but the surface asperities have started to interact. [30] For film thicknesses such that $1 > \Lambda$, many of the asperities come into contact, generally generating heat and causing asperities to break off in this 'boundary' regime. However, in some cases, the lubricant can be chemically active and can combine with the surface to form an extremely resistant surface, with a very low friction coefficient. [3] The dependence of the friction coefficient on chemical composition, rather than viscosity and density, opens up a whole new domain for tailoring the friction coefficient in this boundary regime.

1.2.1 Polymer Brushes

The most common type of joint in mammals is the synovial joint. [29] It has a remarkably low friction coefficient on the order of 10^{-3}, and is used for up to

80 years with impressively little degradation. [31] This is remarkable because all of their properties - the joint surfaces are microscopically rough (˜$1\mu m$ asperity heights), the lubricating fluid is mainly made from water, so its viscosity is very low and the relative velocity between limbs is slow - should yield a very high friction coefficient. [3, 31] What other properties make this lubricant so effective?

In addition to water, the lubricant also contains hyaluronic acid and some proteins. [31] The acid helps slightly by increasing the viscosity a little, but the proteins are the real key for boundary lubrication. [32] They consist of a polypeptide chain with side anionic oligosaccharide chains. These chains (known as polymer brushes) retain water due to osmosis even under very high pressures, which explains why water can be used as a lubricating fluid despite its low viscosity. In addition, other proteins can embed themselves in the cartilage, stiffening the contact. [31] Finally, the water can transfer heat effectively due to its high effective heat capacity.

Using this naturally occurring polymer brush template, synthetic brushes are being developed. [33–36] They generally consist of a surface with a high density of polymers grafted on the surface, while the other end is free to interact with the other surface in liquid. With a high density of brushes, the surface can sustain high pressures due to the entropy differences inside and outside the brushes.

Using statistical mechanics, the root mean squared radius, or the Flory radius, R_F of a single chain in three dimensions is: [37–39]

$$R_F \cong aN^{3/5} \tag{1.6}$$

where a is the statistical segment length and N is the degree of polymerization. Now, for multiple chains, the distance between chains is

$$L = \frac{a}{\sqrt{\sigma}} \tag{1.7}$$

where σ is the grafting density. Substituting this equation into equation 1.6 yields:

$$\frac{1}{N^{6/5}} \cong \left(\frac{L}{R_f}\right)^2 \sigma \tag{1.8}$$

Low grafting densities are when $\sigma < 1/N^{6/5}$, and high grafting densities are when

$\sigma > 1/N^{6/5}$. When the polymer densities are high, osmotic pressure and electrostatic forces force the chains to extend, while the elasticity of the polymers prevent them from completely straightening. [40] From these considerations, the brush height in general is given by: [41, 42]

$$h = Na\omega^{1/3} \tag{1.9}$$

Using polymer brushes, it has been shown that it is possible to tune adhesion, lubrication, wettability, viscoelasticity and friction. [43–46] The goal of this study is to use an AFM for friction characterisation to investigate a novel polymer brush system with uniquely high brush densities.

2

Atomic Force Microscopy

Atomic force microscopy (AFM) is a local probe technique with extremely high resolution on the order of a few angstroms. This is 1000 times smaller than the visible light diffraction limit, and has comparable resolution to scanning tunneling microscopy (STM) and transmission electron microscopy. It was invented by Binnig et al. in 1986 for which they received the Nobel Prize for Physics that same year. [47] In addition to its surface imaging capabilities, it can be used to manipulate matter and measure surface properties on the micro- and nano-scale.

The probe consists of a sharp tip on the free end of a cantilever. The cantilever is a micron sized flexible beam with one end rigidly attached to a substrate and the other end suspended over the sample. The suspended end is force sensitive and interacts with the sample through the tip. Manipulation of the tip with respect to the sample is achieved through extremely small, accurate and precise movements performed by piezoelectric elements. A coarse adjustment motor is employed to bring the tip down from multiple millimetres of separation into initial contact or to within about 1 micron of the surface. Once in contact, the surface forces F induce a deflection x on the free end of the cantilever with stiffness k which can be measured by Hooke's law: $F = kx$. Deflection measurement is usually achieved by optical beam deflection into a position sensitive photodiode, [48] though interferometry while capacitive sensing and piezo-resistive sensing techniques are also used. Deflection measurements by optical beam deflection measure the cantilever deflection as a change in beam position on the photodiode. The photodiode voltage can then be compared to a user-determined value and used to adjust the tip position as desired.

2.1 AFM Instrumentation

2.1.1 Bioscope Atomic Force Microscope

All AFMs share the same basic characteristics, but depending on the application, vary significantly in functionality and design. The main microscope used in this study is a Bruker (formerly Digital Instruments) Bioscope AFM, made for use in the life sciences and is shown in figure 2.1. The Bioscope consists of an AFM head on top of an inverted optical microscope. The sample is accessible from the top for force microscopy and from below by the optical microscope for various optical cellular imaging capabilities and for easy alignment of the cantilever on the sample. The cantilever has to be scanned over the surface rather than scanning the sample with respect to the cantilever because the microscope and stage together are too heavy to move on one piezo and because the stage cannot move with respect to the microscope once imaging begins. There are some advantages and disadvantages of scanning your tip rather than your sample.

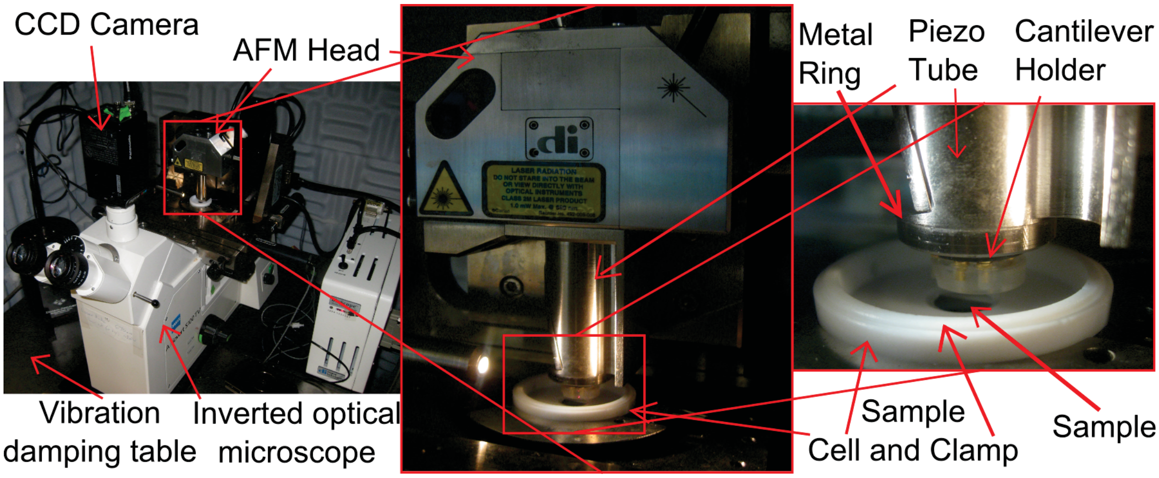

Figure 2.1: The Bioscope AFM.

Since the tip is being moved with respect to the laser, the laser focus has to move with the cantilever as shown in the Bioscope AFM head schematic in figure 2.2. This is accomplished with a tracking lens which sits inside the piezoelectric tube. However, the path length of the laser must change and introduces non-linearities and interference patterns in the laser signal. The lens requires very precise positioning, so extended use or any damage to the piezoelectric tube will likely introduce some tracking lens errors, necessitating frequent replacement. One advantage of scanning the tip over scanning the sample is that the microscope can accommodate large samples (eg. cells in a petri dish or a sample with lots of liquid). The reason for this is that piezos lose significant bandwidth when actuating large loads. [49]

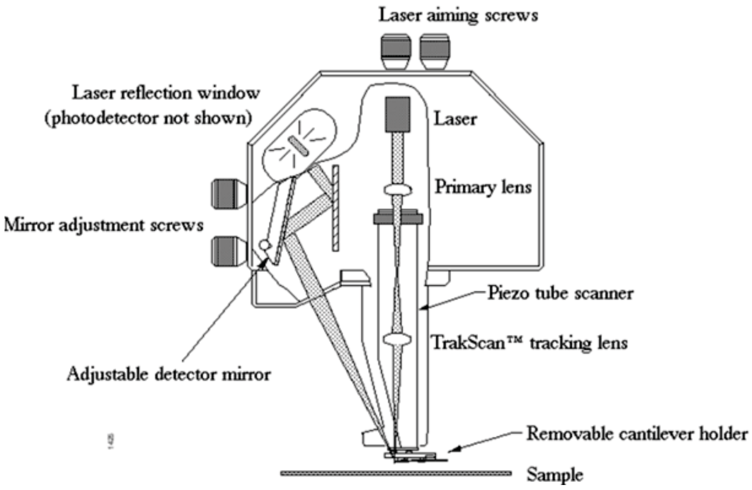

Figure 2.2: Bioscope AFM head (adapted from Nanoscope IIIa manual)

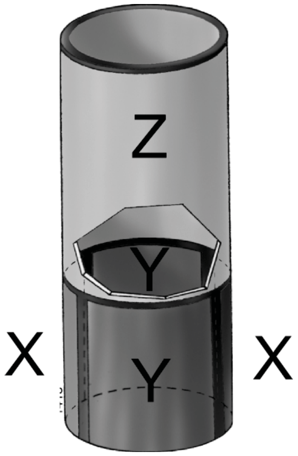

Figure 2.3: Schematic of the Bioscope x-, y- and z-piezos

2.1.2 Instrumentation Limitations and Noise

Given the precision desired while using the Bioscope, noise is minimized whenever possible. The Bioscope has intrinsic and situationally dependent noise limitations that are important to understand while evaluating the measured precision. External noise is at all times minimized in an attempt to attain the highest possible precision.

The lateral (x and y) and vertical (z) piezoelectric scanners (piezos) (depicted in figure 2.3) can have positioning accuracies to within 5Å and 1Å respectively. Unfortunately non-linear properties affect their accuracy. Some of these non-linearities do not depend on time, so can be better calibrated and eliminated.

The piezo extension and retraction respond non-linearly to voltage. These non-linearities are calibrated to 2nd order in the z-piezo and to 3rd order in the x- and y-piezos. This non-linear response in the y-piezo movement can be seen in figure 2.4. There is also coupling of the voltage between scanners. This is calibrated between the x and y piezos, but the z is relatively independent and is thus left uncalibrated. These static non-linearities lead to an approximate error of 15nm over 1μm, but the relative error increases with decreasing scan size. Time dependent non-linearities are a bigger problem because their calibration is much more difficult. Piezos are made from viscoelastic material which causes it to creep or relax after a scan. This means that although the strain on the piezo (the voltage) is kept constant after a scan, the strain will continue to increase (creep) or it will start to decrease (relaxation) on its own. Initially creep is quite significant, but it will decrease until it is almost negligible after about 2 minutes. [50] Creep is minimized by the user by using small scan sizes over short periods of time.

The cantilever deflection x_N caused by an applied stress s is given by Stoney's formula $x_N = (3s(1-\nu)L^2)\,/\,(Et^2)$ where ν, E, L and t are the cantilever's Poisson ratio, Young's modulus, length, and thickness respectively. By dividing this by the force, an effective spring constant k_N can be obtained by $k_N = (Ewt^3)\,/\,(4L^3)$ where w is the cantilever width. In the life sciences, smaller cantilever spring constants are often desired so as to not damage the sample by the application of excessive force. Cantilevers are normally fabricated using silicon or silicon nitride because they are convenient materials for microfabrication. Although they have comparable Young's moduli, silicon nitride is preferred in biological applications because it is easier to manufacture thinner cantilevers, yielding a smaller spring constant. Our cantilevers' spring constants were generally specified to within about 10$\%$, but the cantilever spring constants can be easily calculated to under 4$\%$ error using the Sader Method as described in Chapter 4. [51] Similarly to the flexural cantilever dynamics, the angle of twist θ caused by a torsion T is $\theta = TL/GJ$ where G is the shear modulus and J is the torsion constant. The torsional spring constant is thus given by $k_N = Gwt^3/3Lh^2$ where h is the tip height. The cantilever's torsional properties are usually not specified by the manufacturer because they are harder to control. However, using the torsional Sader method, the torsional spring constants have all been measured to within 9$\%$ error. [52]

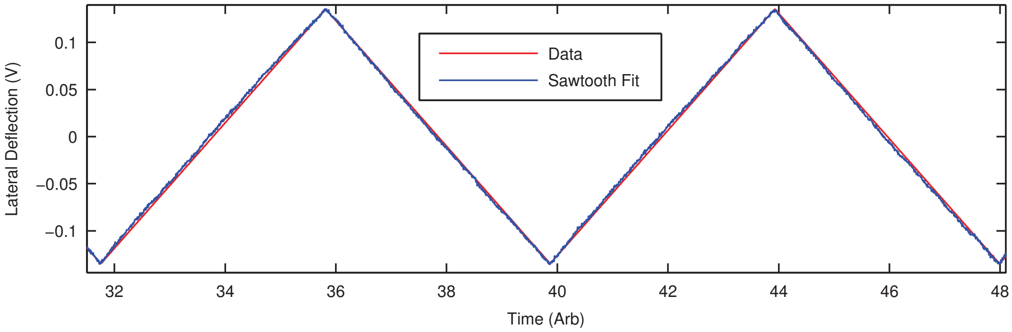

Figure 2.4: The non-linear response of the piezo to a stress (applied voltage across the piezo). A tracking lens error allows this visualization to be possible. If no non-linearities were present, the data would be a perfect sawtooth, following the sawtooth fit.

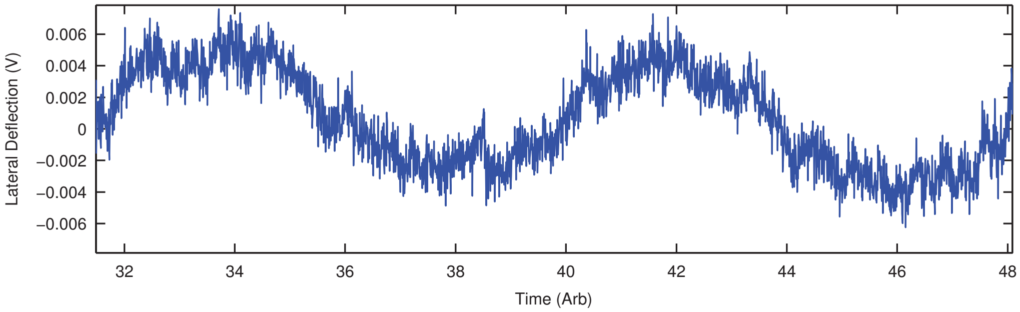

Figure 2.5: These data are the residual of the non-linear piezo response after being subtracted by the sawtooth fit in figure 2.4. The non-linearities of the piezo are shown as the deviation from a flat line at 0 lateral deflection.

The Bioscope uses an optical beam deflection technique to measure cantilever deflection. The smallest detectable change in laser position on the photodiode is about 1mV in a 1Hz bandwidth. Converting this voltage deflection into a cantilever deflection requires a calibration step which depends on the cantilever lever arm and total signal on the photodiode. This conversion is known as the deflection sensitivity, and typical values are around 100nm/V. This gives a measurement sensitivity of $1\AA$. Given a typical spring constant of 0.1N/m for the life sciences, the force sensitivity is about 10pN. However, silicon and silicon nitride are both translucent for thicknesses of $\tilde{}0.5\mu m$. This means that the top of the cantilever is coated with gold to allow optical reflection. Unfortunately these materials have different thermal expansion coefficients. When laser light heats the cantilever, this can cause deflections of up to 10nm for temperature changes as small as 0.001˚C. [53, 54] The cantilever temperature can be increased by 10˚C in air and 3˚C in water and reaches equilibrium after about an hour. Temperature stability throughout experiments is thus very important while other sources of heat such as the illumination light and the heated stage must be minimized. For this reason, the stage is made from a heavy and thermally stable material called invar.

Cantilevers act as harmonic oscillators with resonant frequencies ω_r given by $\omega_r = \sqrt{k/m_{effective}}$, so those used in biological applications that have small spring constants will also have low resonant frequencies. These resonant frequencies are on the order of 10kHz so they are particularly sensitive to low frequency noise such as mechanical and acoustic vibrations. The microscope is located in the basement of the WONG building at McGill University on a separate foundation from the rest of the building on top of a vibration-damping table inside a box with acoustic isolation to minimize noise from the rest of the building, to decrease the frequency and magnitude of any perturbations and to minimize acoustic vibrations respectively.

2.2 AFM Methods

Atomic force microscopy measures only forces. It is such a diverse tool because, depending on the tip and sample, the nature of these forces can vary widely. Measuring the mechanical contact force while raster scanning the tip along the surface will give a topography image. Scanning out of contact can give information about the sample's electrostatic force. Depending on the experiment and the nature of the tip-sample interaction, many different forces can be measured (eg. intermolecular and intramolecular, electromagnetic, frictional, the mechanical contact or normal force, etc.). Typically there are two ways to obtain information about the forces in the sample and/or tip: Raster scanning the tip over the sample (scope trace) or pushing the tip into the sample (force distance curve). An example using a scope trace is to obtain a topography image; the tip is usually held at a constant z-position relative to the sample to avoid pushing too hard into the surface when passing over varying sample heights. This is accomplished by using a feedback loop which compares a user-entered value (the setpoint) with the photodiode voltage, and then by extending or retracting the z-piezo accordingly.

2.2.1 Scope Trace Friction Force Microscopy

To measure the friction properties of a sample, the cantilever is moved laterally along the surface, friction resists the tip's motion and causes the cantilever to be torqued rotationally such that the laser is deflected laterally on the photodiode. To begin, the tip is first brought into stable contact with the surface, and a topography image is acquired. A friction measurement is then obtained by actuating the y piezo instead of the regular x-piezo actuation so that the cantilever is scanned laterally. After performing a sufficient number of scope traces for statistics, the normal load is increased by increasing the vertical deflection setpoint. The friction data can then be compared to the topography image in order to find different friction regimes. An example of a friction scope trace is in figure 2.6. Each scope trace gives a friction signal in terms of the lateral deflection on the photodiode, while the normal load is given by the vertical deflection setpoint. Via a suitable calibration, both the lateral and vertical deflection voltages are converted to friction and normal forces in nN. The friction force is then plotted against the normal force to obtain the friction coefficient.

2.2.2 Force Distance Curves

A force distance curve measures the tip-sample forces while the tip is moved in and out of contact with the surface. Depending on the dominant forces present, all parts of the force distance curve profile can vary drastically. Fortunately the strength of these forces have different dependences on tip-sample separation, so it is often possible to identify and quantify these forces. A force distance curve will typically display a sequence of different types of forces, detailed in figure 2.7. Before coming into contact with the surface, long-range electrostatic (or magnetic) forces can be seen, either as a repulsion or attraction. These are followed by short range intermolecular forces, which can further repel the tip or attract it by causing it to jump into contact (eg. Van der Waals forces). Once in contact with the surface, the tip will be repelled by hard Pauli repulsion or by the material's viscoelasticity. These interactions continue during retraction of the tip until the tip

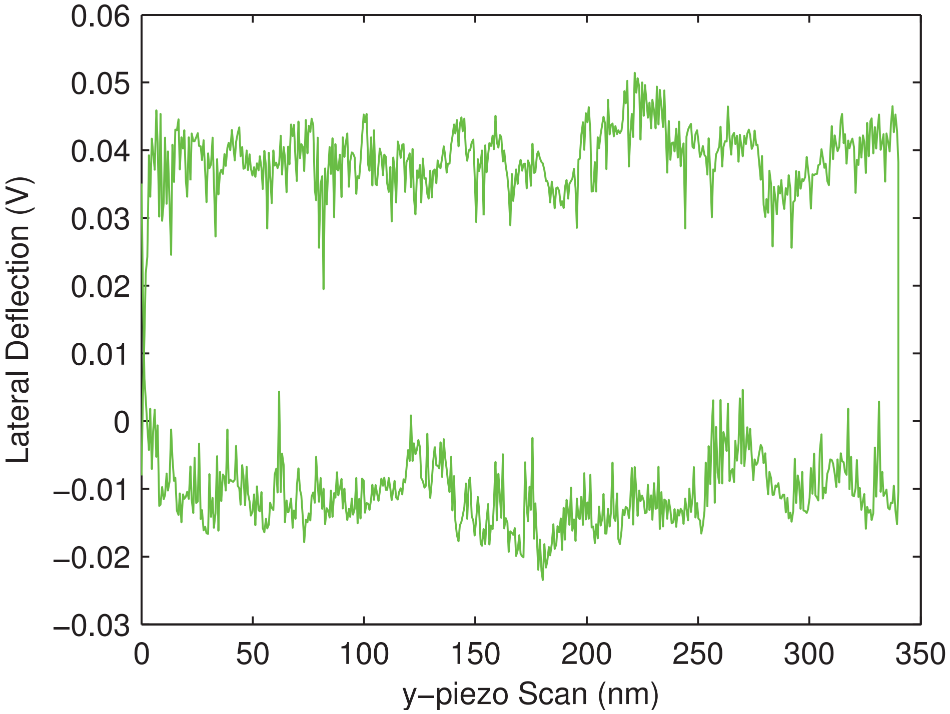

Figure 2.6: Friction scope trace made at a normal load of 23nN (-1V setpoint) for a silicon nitride tip on a GaAs surface. These are data from one scope trace.

has separated from the sample. During contact, the tip will likely have adhered to the surface through a number of different interactions which can be seen by an attractive force that continues past the initial contact point until the cantilever restoring force overcomes the adhesive force and is released.

The long range electrostatic interactions are due to Coulombic interactions which has an inverse square dependence on distance. It is sometimes possible to minimize them by neutralizing the surface using a de-ionizer. This operates by modifying the Debye screening layer by charge concentration (ie. molarity) and ionic strength (ie. the single and doubly charged ionic species). Intermolecular forces such as Van der Waals and dispersive forces start to dominate over electrostatic forces as the tip-sample distance is decreased because they exhibit approximately an inverse 7th power dependence on separation. [55] In saline solutions, both of these longer range forces are usually negligible. In the Lennard-Jones potential

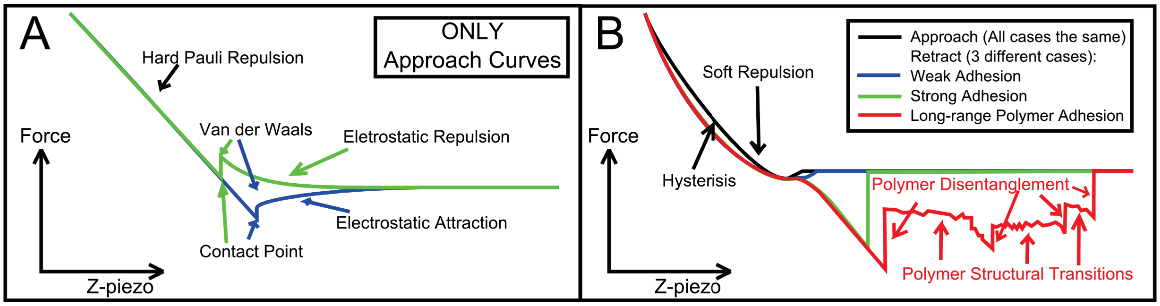

Figure 2.7:
A. Electrostatic repulsion vs. attraction approach curves on a hard sample. They are much longer range forces than Van der Waals forces which can be seen in both cases as the cantilever snaps into contact with the surface. Once in contact, hard Pauli repulsion dominates the interaction, and both curves have the same linear behaviour. These curves are an adaptation of approach curves from the Nanoscope manual, but have also been observed experimentally.
B. Approach and retract curves on a viscoelastic sample. In the approach curve, all the cases presented here are quite similar. However, during retraction, weak and strong adhesion can be distinguished because the cantilever is held further below its setpoint in strong adhesion. Long range polymer adhesion can be identified by an interaction which has many jumps due to structural transitions or disentanglement of the polymer. These curves are depictions of data frequently seen in these experiments.

model, intermolecular forces are the attractive term.

Once the tip is said to be 'in contact', Pauli repulsion dominates the interaction. This is the repulsive term in the Lennard-Jones model and has an inverse 13th power dependence on separation. Pauli repulsion is due to the fact that electrons cannot occupy the same quantum state simultaneously, so each sample's electrons repel each other. The repulsion acts equally to apply stress on the internal structure of the material. The result in a rigid material is that the tip will be deflected equal to the z-piezo movement, and the sample will remain relatively unstrained as in figure 2.7A. However, if the material is viscoelastic, it will be deformed, and the resultant force distance curve will be non-linear as in figure 2.7B. The elastic deformation depends on the strength of covalent and ionic bonds formed between the sample's atoms, usually along specific crystallographic planes, displaying a similar response to a combination of springs. [56, 57] The elastic response thus is dependent only on the displacement from equilibrium. The viscous deformation is caused by the diffusion of atoms within the solid of an amorphous solid. A viscous material's response to strain is time-dependent as well as dependent on the magnitude of the strain. The material thus displays a hysterisis between the indentation and retraction curves as the material continues its response to the initial deformation as in figure 2.7B. The hysterisis can be minimized by making the scan rate as slow as possible since viscous damping is proportional to the deformation rate. Polymers are known to be viscoelastic, so the force distance curve scan rate was usually minimized to take 100 seconds.

Adhesion between the tip and the sample is generally caused by mechanical, chemical, dispersive, electrostatic or diffusive adhesion. The most important of these forces is usually dispersive adhesion, which includes attractive forces such as London dispersion, Keesom, Debye and Hydrogen bonding. This adhesion force manifests as an extension of the retraction curve past the set point. In the case of polymers compressing polymers, diffusive adhesion can be important because the polymers become intertwined and resist separation. This can cause structural polymer transitions and polymer disentanglement shown in figure 2.7B. Usually adhesion is some combination of Van der Waals, electrostatic, hydrophobic/hydophillic or capillary forces, but it is hard to determine which one is dominant.

2.2.3 Featured Technique - Friction Force Distance Curve Microscopy

Standard friction force microscopy (FFM) is performed using the scope trace method (STFFM) as described in section 2.2.1. There are a couple of difficulties with STFFM which limit the technique. Firstly, the method is very slow because a friction measurement needs to be performed for each normal load. This means that it is very difficult to measure frictional properties in unstable systems. For example, certain levels of pH are not sustainable over long periods of time when exposed to air. Solutions with a volume of about 5ml are only stable for around 1 hour. Given that it can take about 2 hours to make multiple friction measurements at different normal loads, obtaining multiple sets of data can be impossible in unstable conditions and very tedious in others. Another difficulty with STFFM is in determining the absolute normal load applied. This is in part due to adhesive forces which apply additional forces to those exerted by Paul repulsion. There could also be virtual deflection due to laser interference or drift which can cause over or underestimation of the deflection. These can both be easily identified through force distance curves, but are not measurable using STFFM.

A novel friction force microscopy technique has been developed where multiple friction loops are performed during a force distance curve, here named friction force distance curve microscopy (FFDCM). Each friction loop (lateral scan) is equivalent to a scope trace and gives a frictional force while the normal load is increased as in a normal force distance curve. Both the lateral and vertical deflection signals are acquired simultaneously. A full friction force distance curve (FFDC) can be performed in seconds. In order to get multiple scope traces per FFDC, the z-piezo scan speed must be adjusted to the frequency of the lateral scan. FFD curves obtained in just 100 seconds with large scan sizes of 250nm and slow scan speeds of 500nm/s give a total of 50 full lateral scans for 1 force distance curve. Our data acquisition card allows 64000 points per scan (min frequency ~1Hz), which gives 640 points per scan lateral scan. Even given this large scan size and slow scan speed, FFDCM measurements can be obtained in less than 2 minutes, which is still 60 times faster than typical operation times using the STFFM method. A full friction measurement is easy to take multiple times in order to get good statistics and verify repeatability.

FFDCM measures both the vertical and lateral signals simultaneously, giving a friction measurement for all corresponding points on the force distance curve. This allows for easy absolute determination of the normal load because the adhesion forces are easily identified in a force distance curve. The force distance curve also allows for easy identification and subtraction of the virtual deflection slope to obtain the real normal load for all friction points. In addition, having a friction measurement for every normal load measurement allows a continuous measurement of friction. If there is an important event identifiable in the force distance curve which affects the friction, it should be evident by a kink in this continuous measurement.

The STFFM method allows viewing of features in each scan because each scope trace was seen in real time. Differences in low and high friction regions could also be identified in these scope traces. This is still possible in the friction

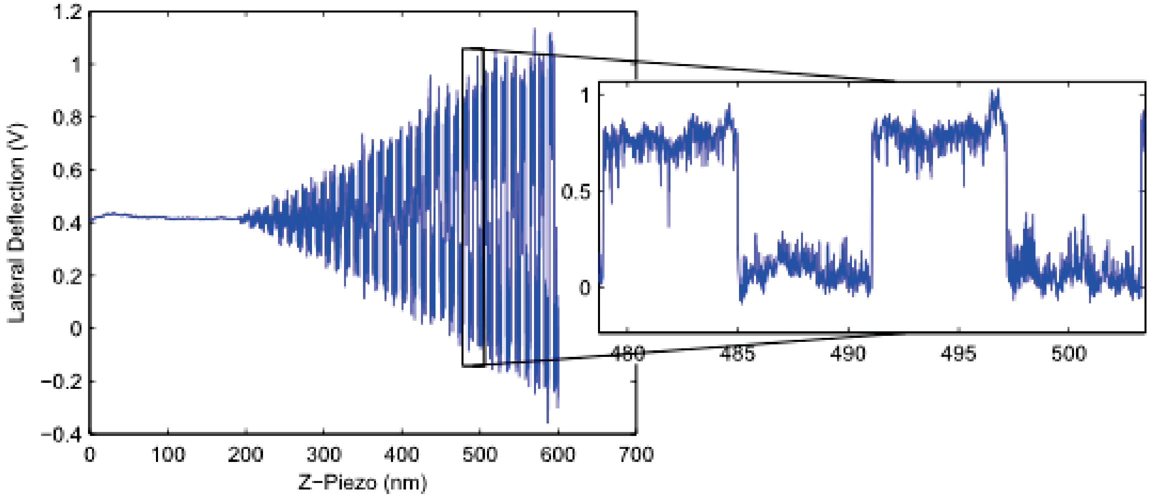

Figure 2.8: Friction force distance curve for a silicon nitride tip on a GaAs surface. Two scope traces are zoomed to show the details of each scan to be able to compare with the friction scope trace in figure 2.6.

force distance curves by zooming in on each scope trace as seen in figure 2.8. In order to verify that the FFDCM and the STFFM methods were equivalent, friction measurements were obtained for two different samples using both methods, and are shown in figures 2.9 and 2.10. Both curves have the same friction coefficients within the uncertainty of the experiment. Both curves appear to be slightly offset. This can be attributed to the fact that the absolute value for the normal load cannot be measured using the STFFM method. However, both curves display the same friction dependence on normal force.

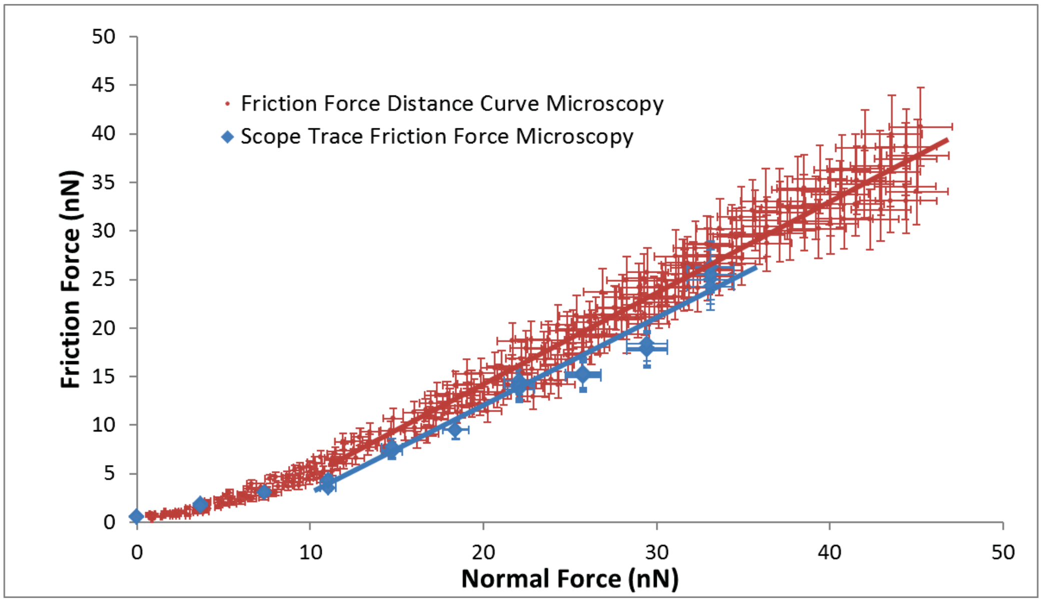

Figure 2.9: The friction force plotted as a function of the normal force for a silicon nitride tip on a GaAs surface in water. The friction coefficient using FFDCM and STFFM are 0.91±0.21 and 0.88±0.18 respectively. Both methods agree within error.

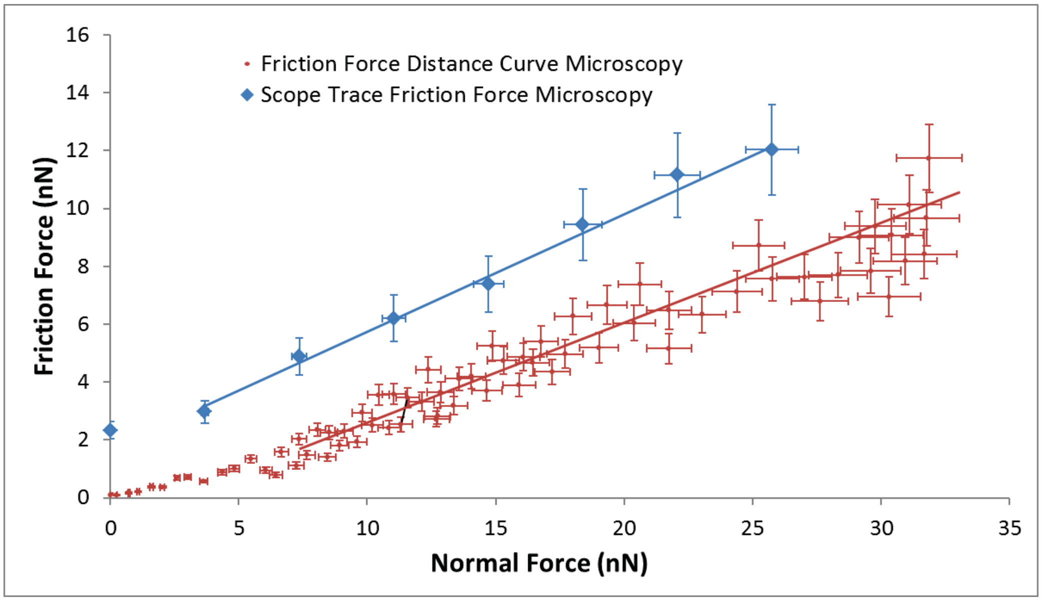

Figure 2.10: The friction force plotted as a function of the normal force for a polymerized bead on a polymerized surface in water. The friction coefficient using FFDCM and STFFM are 0.35±0.12 and 0.4±0.1 respectively. Both methods agree within error.

3

Experimental Preparation and Challenges

3.1 Experimental Preparation

3.1.1 Polymer Grafting Approaches

My collaborator, Olga Borozenko, of Dr. Suzanne Giasson's research group at the University of Montreal has used a grafting-from approach to prepare polystyrene-block-poly(acrylic acid) (PS-b-PAA) copolymer brushes on silica. [58] Polymer brushes are very promising smart materials, and Professor Giasson as well as others have already shown that they can have extremely low friction coefficients. [59–61] When immersed in high pH, the polymer chains are deprotonated, and stretch themselves upwards due to electrostatic and osmotic pressure between them. These swollen dissociated polymers act as a lubricant in the boundary friction regime with remarkably low friction coefficients of about 0.001. The degree of dissociation depends on a number of parameters which can be controlled depending on the material preparation.

The two main grafting methods for attaching polymer chains to the surface are the grafting-to and grafting-from approaches. [62] The problem with the grafting-to approach is that the end-functionalized polymers must be pre-synthesized. This causes unfavourable steric interactions while attaching them to the surface, and prevents high grafting densities. In contrast, Ms. Borozenko uses the grafting-from approach which allows a much higher grafting density by coating the substrate with an initiator and polymerizing from the sample. Radical polymerization methods give control over the layer thickness, architecture and composition. [63–66]

Each layer of the PS-b-PAA sample prepared by Ms. Borozenko is shown in figure 3.1. Most importantly, it consists of a polystyrene (PS) layer that protects the polymer-substrate interface from detaching in extreme pH solution and a poly(acrylic acid) (PAA) layer which is stimuli-responsive. These are about 3.0±0.5nm and 10±1nm respectively, and when stimulated in a basic solution of pH 10.5, the PAA layer extends from 10nm to about 90±7nm. NaCl salt enhances this extension by about 20±5nm for a 10nm layer. This is because the Na^+ ions favor dissocation of weak polyelectrolyte brushes by replacing the protons in the COOH groups. This increases the electrostatic field and the osmotic force between polymer brushes, and thus also the swelling. The stimuli-response takes about 2 hours to reach equilibrium, so measurements were taken at least 2 hours after submersion of the polymers. At pH 10.5 and 9.5, the swelling was only stable for about 2 or 4 additional hours respectively, so measurements were taken quickly using the FFDCM method.

3.1.2 Beading

Often, a standard cantilever tip is not ideal because of tip sharpness, geometry or surface composition. For the experiment, a 4.5μm bead was glued behind the cantilever tip. The bead's larger curvature is preferred because of it's larger sample-probe surface contact area, and relative ease for polymerization compared to the standard tip. Gluing a bead precisely behind the cantilever tip (here called beading) is a difficult task. A tapered pipette is used to deposit glue on the cantilever in order to pick up the bead permanently.

Gluing

The 4.5μm polymerized beads are submerged in solvent, placed on a glass slide and dried using nitrogen to ensure beads do not conglomerate. Presence of the beads is confirmed by identifying them using 40x magnification, and then positioned on the Bioscope stage, ready for gluing. A tapered pipette tip positioned with a micromanipulator is used to apply glue to the end of a rotated cantilever as shown in figure 3.2. The pipette is prepared by heating and pulling it into a tapered tip in a Model P-87 Micro-pipette puller. Obtaining the desired taper and

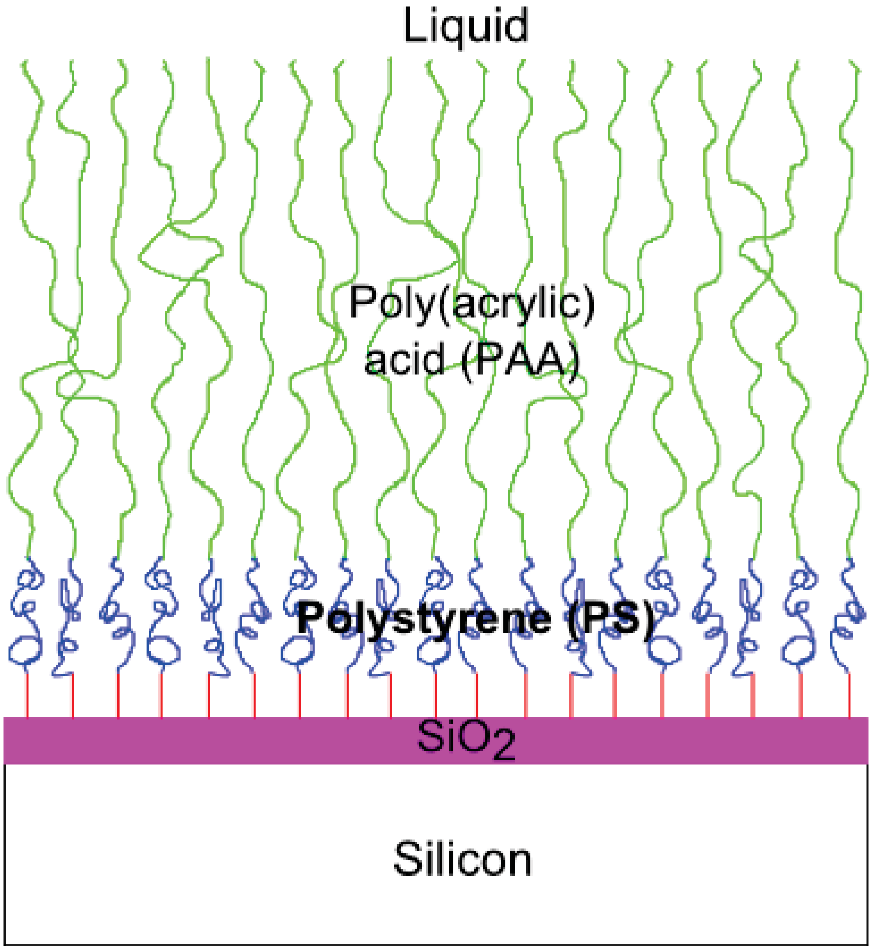

Figure 3.1: Extended polymer brush sample layers when in a basic solution.

tip size requires specific puller parameters of heat, power of pull, velocity, cooling time and pressure.

If the pulled pipette tip is too large, too much glue will be picked up and subsequently deposited underneath the cantilever. One solution to this problem is to use compressed gas to blow most of the glue up the pipette, leaving only a small layer on the end of the pipette, but it is hard to control how much is leftover. If the pipette tip is too small, the glue will prefer to sit further up the pipette such that the pipette tip will make contact with the cantilever, preventing deposition of the glue behind the tip. Also, due to the pipette's smaller surface area, most of the glue will prefer the cantilever, and too much glue will be deposited. The optimal diameter of the pulled pipette end was found to be about 5-10μm for picking up 4.5μm beads. Finding the correct size is difficult as too much glue engulfs the bead, and too little won't pick it up.

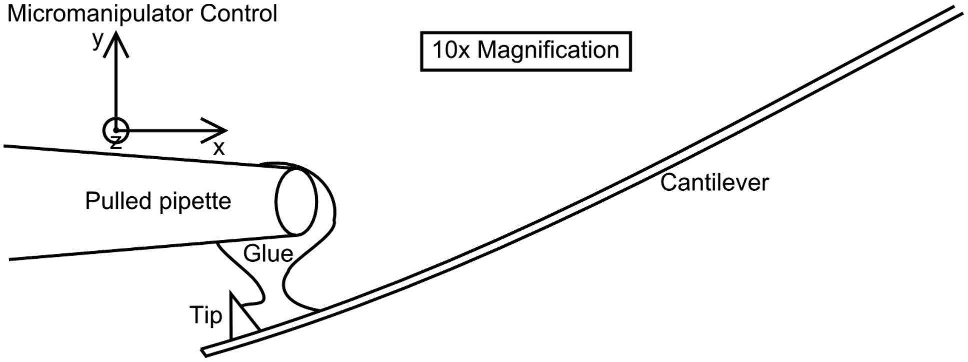

Figure 3.2: A pulled pipette is being micromanipulated to apply glue to the cantilever which is anchored through its substrate sideways in sticky puttee. As the pipette is pulled away, the cantilever flexes with it until its restoring force becomes strong enough to pull away with some glue.

Glue

The most important consideration for the gluing of the polymerized bead to the cantilever is its viscosity. If the glue is too viscous, too much can get onto the underside of the cantilever and it can engulf the bead or the glue will prefer the glass slide to the cantilever because of its larger surface area. It must also be viscous enough that the glue can pick up the bead and keep it localized behind the tip. Beading with a heat curing epoxy called EPOXY 353ND was attempted, but it became too viscous before picking up the bead. TorrSeal was used to pick up larger beads, but 4.5μm beads were too small and the glue too viscous, such that the glue would be lost on the slide. Of the glues that were tested (ELC 4481 Light curing Adhesive, E-30CL Loctite epoxy, Varian TorrSeal Resin and EPOXY 353ND), the best one was E-30CL Loctite epoxy. Although the light curing adhesive also worked and is convenient because of instant curing, UV light is known to damage polymers, so it could not be used to glue a polymerized bead. The epoxy had a viscosity of 6Pa$\cdot$s which has turned out to work extremely well for beads of all sizes tested (4.5-60μm).

Bead Size

4.5μm and 60μm beads were used in our experiments. 4.5μm beads are difficult and inconvenient to use because some cantilevers have tips larger than 4.5μm, the beads are hard to distinguish from other particles under 10x magnification and they are difficult to glue right behind the tip as they cannot be seen under a cantilever of 40μm width and the cantilever approach doesn't appear linear in the optical microscope. Fortunately, beads can be distinguished from other particles by looking for bead conglomerations. The bead is glued in the correct spot behind the tip by following an easy procedure: the tip is brought down to the slide, and it's position is marked on the optical microscope screen. It is then retracted, and the bead is re-positioned in that point on the screen for pick-up.

Beading Summary and Complications

The reliability and rapidity of this now 2-3 hour procedure has been improved dramatically by refining these techniques and in particular by applying glue to multiple cantilevers in parallel by holding them sideways in sticky puttee. The old method was much slower and riskier as only one cantilever could have glue applied at a time because the cantilever was held in tweezers and placed in sticky puttee sideways, and it would often fall out and break. A 4.5μm bead can be seen glued to a cantilever in figure 3.3

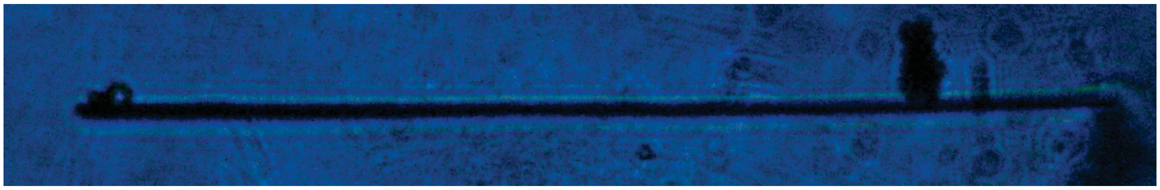

Figure 3.3: A 4.5μm bead has been glued behind the tip of this ORC-B cantilever from Bruker, seen under under 40x magnification.

3.1.3 Sample Cell

The measurements were performed in a range of pH's and salt concentrations to allow the swelling of the polymer brushes. An inert Teflon sample cell and Teflon sample clamp compatible with the heating stage of the AFM set-up were machined to hold aqueous solution and the sample stationary while still allowing the AFM cantilever access to probe from above as seen in figure 2.1, chapter 2.1.1. Polymer-solution equilibration takes a minimum of 2 hours. Taking multiple friction measurements for good statistics and performing other surface characterizations takes (barring complications) about an additional 30 minutes, meaning that a full set of measurements takes a minimum of 12.5 hours (5*2+5*.5 = 12.5). The last measurements performed are at pH 9.5 and 10.5 because it takes much longer than two hours for the solution to equilibrate if the pH is decreased rather than increased. However, pH 9.5 and 10.5 solutions are unstable if left overnight, so if any complications arise during their measurement, the experiment time could become significantly longer than 12.5 hours. Rather than rushing the experiment in one very long day, each set of measurements was performed over a period of two days, beginning the second day in pH 9.5 solution. The sample cell was thus made large enough to avoid overnight evaporation.

3.2 Experimental Challenges

3.2.1 WONG Flood

On January 28th, 2013, a pipe burst next to the WONG building (McGill University) which flooded the lab with about 4 inches deep of water and delayed work by exactly 2 months. During this time, the lab was cleaned, equipment was moved, many discussions and meetings were had and the equipment's functionality was tested.

3.2.2 Malfunctioning Bioscope

When the Bioscope is in 'tip voltage mode', it attenuates its data acquisition range by 8 times to a range too small for friction force distance measurements. To disable this 8x attenuation, it is necessary to switch a jumper cable inside the Z-board, set the range to 20V in the Nanoscope software and to set a switch away from analog 2 on the extender module. Unfortunately this last step is in a separate manual, so the conclusion after fixing the first two was that something in the hardware was broken. This prompted a lengthy troubleshooting effort where the Z-board, Extender Module and Nanoscope IIIa Controller were partly reverse engineered. After replacing a number of blown resistors in the Z-Board, and the hardware was re-assembled, the microscope stopped working properly, displaying a ”Not responding - - Retry” error. The manufacturer technical support had many suggestions which didn’t help. Fortunately the lab has much of the same hardware on another AFM which was systematically substituted into the broken system to find out that a cable inside the Controller was broken. Though this didn’t help with any particular project, the lab now has a partially filled electronics diagram of much of the microscope, a more detailed reference for the signal outputs in the Bioscope’s alternate configurations (in a table in appendix A) and the 8x attenuation problem was finally fixed as well.

3.2.3 Cracked Piezoelectric Actuator

The piezoelectric actuator (piezo) in the Bioscope is more vulnerable than in most AFM’s because the cantilever holder is attached directly to the end of the piezo. The z-piezo has cracked on four separate occasions as seen in figure 3.4. The first was the re-opening of a crack from a previous user, and was glued back together using Krazy Glue. The second was the re-opening of the same crack, but this time the piezo broke completely, and was not glued completely flush. The third and fourth were re-openings of the second crack with slight deviations, and was fixed using an epoxy. After these breaks, there have been some issues with the AFM including a tracking lens error which is corrected for as outlined in section 4.3 and the laser path being clipped. The piezo will now be replaced, but these quick fixes were done in the interim in order to finish my thesis because piezo replacement times can be quite long.

Tracking Lens Error

Unique to the Bioscope AFM is a lens inside the piezo tube called the tracking lens which keeps the laser focused on the same spot on the cantilever even though the x- and y- piezos move the cantilever laterally during imaging. There is

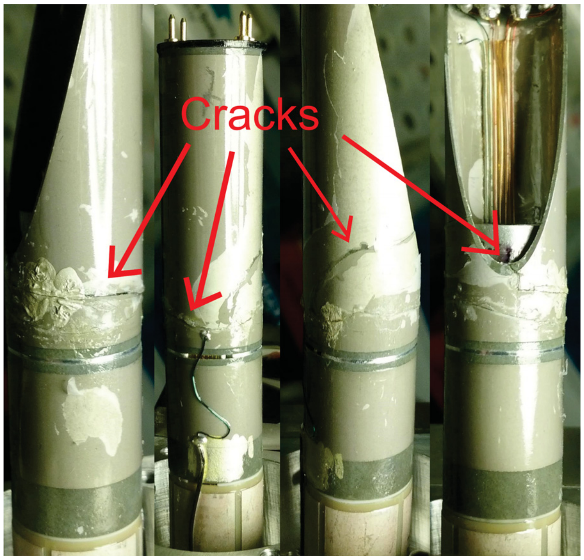

Figure 3.4: All 4 sides of the z-piezo are shown in these pictures. There is one main crack which goes all the way around the piezo, caused by a complete dislocation, and a couple of other side cracks. The blotches reaching across the cracks are silver paint for re-connecting the piezo electrically.

a slight kink in the piezo tube due to the cracks such that the position and angle of the cantilever with respect to the tracking lens and laser source has changed slightly. When the cantilever is now moved with respect to the laser, the tracking lens no longer applies the right correction. For y-piezo scans (friction scans) of about 340nm, the horizontal deflection signal oscillates by about 0.36V as seen in figure 3.5. This error in the signal increases with scan size, and is also minimally present in the vertical deflection signal. Fortunately, the error is approximately linear with piezo movement, so it can be systematically subtracted from the data.

Laser Path Clipped

The relative position of the cantilever with respect to the laser source and tracking lens changes the beam path to the photodiode. Now, depending on the position of the cantilever in the holder, the reflected beam can be clipped by a metal ring which is part of the AFM head as shown in figure 2.1. To avoid this, and because of differences between cantilevers and their substrates, each cantilever needs to be positioned differently in the holder. In some cases, it is impossible

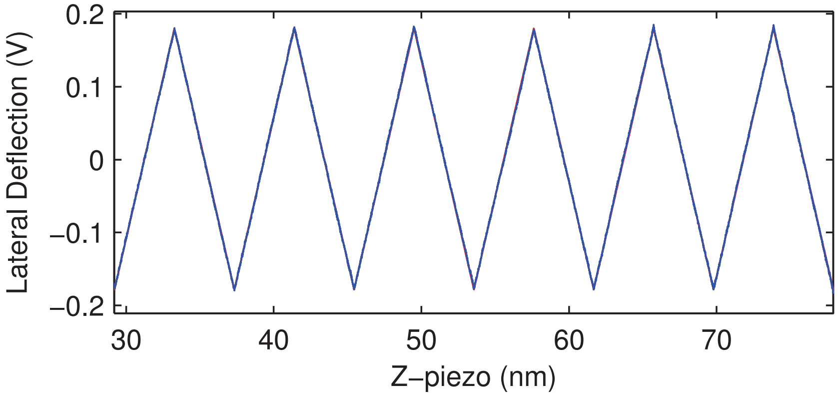

Figure 3.5: Tracking lens error during a 340nm 90° scan.

to position the cantilever in the holder such that the beam is not clipped so these cantilevers can no longer be used.

4

Friction Calibration and Data Analysis

Dividing the lateral force F_L by the normal force F_N gives a measure of friction called the coefficient of friction: $\mu_k = F_L/F_N$. Scanning the AFM tip laterally along the surface induces a torque in the cantilever which is measured as a lateral deflection on the photodiode x_L. The normal force applied during the experiment is measured as a vertical deflection on the photodiode x_N. Calibration in friction force microscopy consists of converting those lateral and vertical deflection voltages into forces in nN by obtaining the calibration factors α and the spring constants k' according to the following equations:

$$F_N = k'_N \left\{\frac{N}{m}\right\} \alpha_N \left\{\frac{nm}{V}\right\} x_N \left\{V\right\} \tag{4.1}$$

$$F_L = k'_L \left\{\frac{N}{m}\right\} \alpha_L \left\{\frac{nm}{V}\right\} x_L \left\{V\right\} \tag{4.2}$$

Where the contents inside {} are the variable's units. The test probe method and Sader method are used to obtain the calibration factors and the spring constants respectively. [51, 52, 67]

4.1 Sader Method

There are a number of methods to obtain the lateral and normal spring constants, but the Sader method has emerged as one of the most convenient and accurate. Most other methods are limited because they require knowledge of the thickness and density of the cantilever which are difficult to control in production and to measure (t is typically measured by STM or a similarly difficult technique). [67]

The Sader method uses the fact that the cantilever's resonant frequency shift from one fluid to another can be modeled. [68] This allows calculation of the spring constant through its planar view dimensions (width w and length L) and the resonant frequency ω and quality factor Q in a fluid:

$$k_N = 0.1905 \rho w^2 L Q_N \Gamma_i \left[\omega_N\right] \omega_N^2 \tag{4.3}$$

$$\kappa_L = 0.1592 \rho w^4 L Q_L \Gamma_i \left[\omega_L\right] \omega_L^2 \tag{4.4}$$

where the contents in [] are a variable's dependent variables. κ_L is the torsional spring constant, ρ is the density of the fluid and $\Gamma_i\left[\omega\right]$ is the imaginary part of the hydrodynamic function, and is only a function of the resonant frequency. [69] w, L and ρ are all easy to measure to a high accuracy without much effort and are specified by the manufacturer. The quality factor and resonant frequencies need to be carefully measured because they can cause a large variation in spring constant determination. These are obtained by modelling the cantilever as a driven, damped harmonic oscillator. The amplitude of oscillation of the cantilever A is driven by thermal motion with amplitude A_d and damped by the medium. It is thus given by:

$$A = \frac{\frac{A_d}{Q^2}}{\left(1 - \left(\frac{\omega_{res}}{\omega}\right)^2\right)^2 + \left(\frac{\omega_{res}}{\omega Q}\right)^2}. \tag{4.5}$$

where in only this equation, ω_{res} is the resonant frequency and ω is the measured frequency. If the resonant frequency is referred to on its own, it is written as ω.

4.1.1 Flexural Mode

To obtain Q and ω_{res}, the amplitude of oscillation as a function of ω, also known as the power spectrum density (PSD), is needed. It is obtained by taking the fast Fourier transform of a thermal spectrum measurement of the vertical deflection signal, with the uncertainty minimized by averaging over multiple PSDs. Since the manufacturer specifies both the spring constant and fundamental reson-

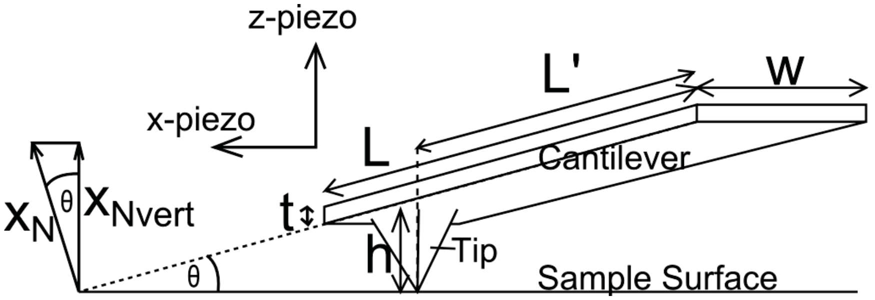

Figure 4.1: Schematic of the cantilever dimensions and tilt.

ant mode frequency, identification of the peak in the flexural PSD is easy. Using Aleks Labuda's Matlab fitting code for a simple harmonic oscillator (re-worked by me and Sebastien Brandenberger) to fit the PSD, the normal spring constant was determined. Each cantilever used in the experiment was fit as in figure 4.2.

The Sader method calculates the spring constant for the full cantilever length L'. However, contact with the sample is made at the tip, so an adjustment is needed. The spring constant has an inverse cubic dependence on cantilever length as shown in Chapter 2's description of cantilever dynamics. The adjustment from the spring constant obtained from Sader's method to the desired spring constant in equation 4.1 is thus:

$$k'_N = k_N \left(\frac{L}{L'} \right)^3$$

Where cantilever dimensions are shown in figure 4.1

4.1.2 Torsional Mode

Unfortunately, the manufacturer does not specify the torsional spring constant or its fundamental resonant mode frequency. Additionally, the signal to noise ratio in the lateral deflection PSD is far worse than the vertical deflection PSD because of the smaller force sensitivity in the flexural modes. As discussed in section 2, the force sensitivity in the flexural signal is over fifty times smaller than that in the torsional signal due to its far smaller spring constant. This makes identifying the fundamental torsional resonance peak in the lateral voltage PSD very difficult. The range of frequencies which contains the peak can be determined by theoret-

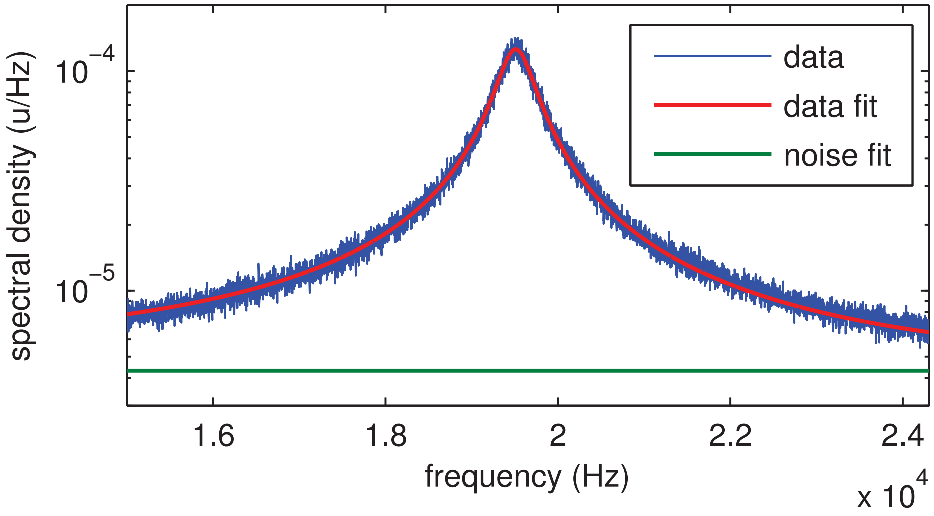

Figure 4.2: Fundamental flexural mode fit in a PSD using Matlab to obtain $Q = 47.3 \pm 0.9$, $\omega = 19.5 \pm 0.2kHz$ and $k'_N = 0.109 \pm 0.003\frac{N}{m}$.

ical calculations following equations by Rabe et al., where the torsional frequency modes ω_n are given by: [70]

$$\omega_n = \frac{2n-1}{2L}\frac{t}{w}\sqrt{\frac{G}{\rho}} \tag{4.6}$$

Where G and ρ are the shear modulus and mass density respectively and have large errors. The fundamental torsional mode can thus be estimated to be between 180kHz and 380kHz. Given this knowledge, a PSD from 0 to 500kHz was obtained (shown in figure 4.3), but it was far too noisy to identify the torsional resonant mode peak.

To increase the signal to noise ratio, a number of noise sources were eliminated. The two most crucial noise sources were from the extender module and from the ground loops between the computer power sources. These noise sources were eliminated by rearranging the microscope into the 'alternate' configuration so that the signal can be accessed before passing through the extender module box, and by putting the data acquisition and operation computers onto the same power source. Although this improved the signal to noise ratio drastically and helped with the eventual fitting, still the resonant peak could not be conclusively chosen as can be seen in figure 4.4.

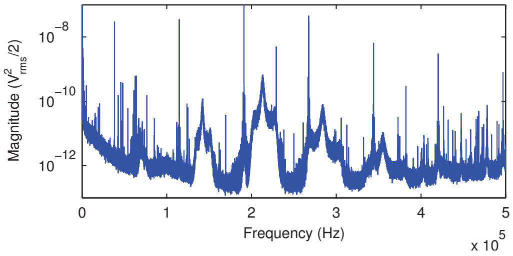

Figure 4.3: Lateral deflection PSD before eliminating the noise sources.

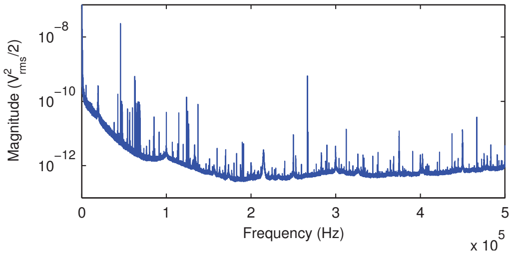

Figure 4.4: Lateral Deflection PSD after eliminating noise sources; most importantly ground loops and the extender module.

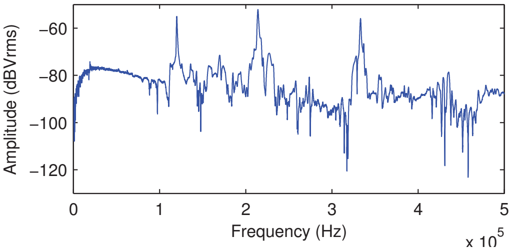

Figure 4.5: Lateral deflection signal as a function of driving frequency using a lock-in amplifier. This is similar to figure 4.4, but mechanical sources are excited, making them bigger. The 3-4 distinct peaks are the normal modes and the fundamental torsional mode.

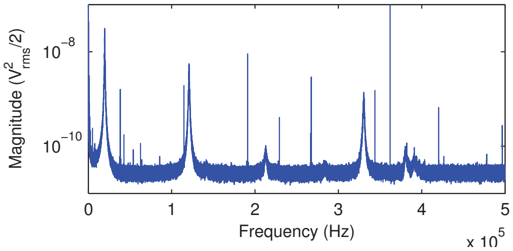

Figure 4.6: Vertical deflection PSD. The first three flexural resonant modes can clearly be seen, as well as the fundamental rotational resonant mode at 214kHz.

In order to isolate the vibrational modes from electronic and other possible noise signals, a lock-in amplifier was used to excite the mechanical modes by driving them. The lock-in amplifier excites the cantilever by oscillating the z-piezo up and down, sweeping through a wide range of frequencies. Although the excitation is in the flexural mode, there is enough coupling between modes to excite the cantilever torsionally as well. The lateral deflection signal as a function of the excitation frequency is given in figure 4.5. From this graph, we can see that there are 3 (or 4) distinct peaks that are significantly larger than the others. The first peak (which is relatively smaller) is at 19.5kHz and we already know it to be the fundamental mode. The other peaks are at 121kHz, 214kHz, and 331kHz. These peaks can all be seen in the vertical deflection PSD as well as in figure 4.6, but the peak at 214kHz is much smaller. According to Rabe et al., the ratio of the fundamental flexural mode to the second and third higher order flexural modes should be 1:6.2 and 1:17.4. [70] For a fundamental flexural mode frequency of 19.5kHz, this predicts second and third higher order modes at 120kHz and 339kHz respectively, so the two larger peaks in figure 4.5 can be concluded to be the higher order flexural modes. The only remaining mechanically excited peak is at 214kHz, and the biggest peak in the lateral PSD in figure 4.4 is also at 214kHz, so it was concluded to be the torsional resonant peak. With the correct peak identified, the fitting code function tolerance had to be increased because the absolute lateral PSD signal was so small. One of the cantilever's fitted curves is shown in figure 4.7.

The Sader Method yields the torsional spring constant κ in $N{\cdot}m$. However, to obtain the lateral spring constant in N/m, it is necessary to adjust for the lever arm of the tip, h by $k_L = \kappa/h^2$. Unlike the inverse cubic dependence of the normal mode spring constant on the cantilever length, the torsional mode spring constant has an inverse linear dependence on cantilever length as shown in equation 2.1.2. The adjustment for the difference between the full cantilever length (measured by the Sader method) and the length of the base of the cantilever to the point of contact thus gives the torsional spring constant from equation 4.2 to be:

$$k'_L = k_L \left(\frac{L}{L'} \right) \tag{4.7}$$

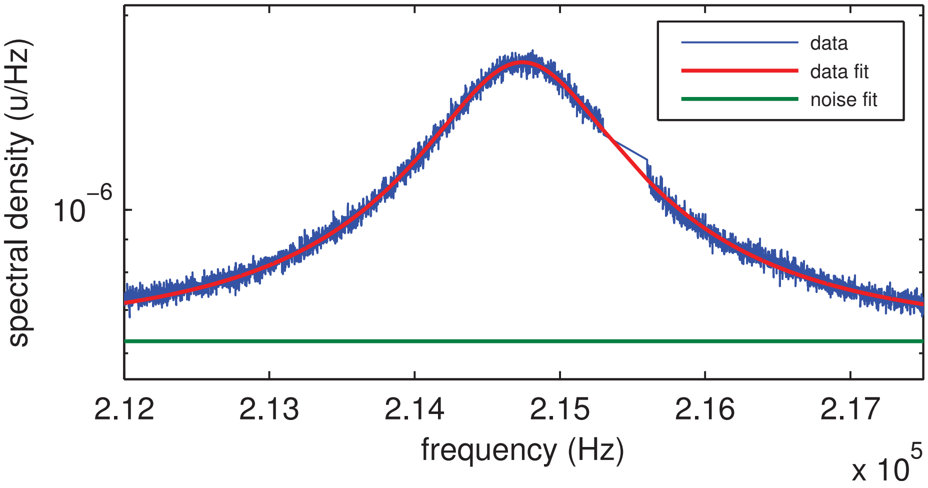

Figure 4.7: Fundamental rotational mode in a PSD fit using Matlab to obtain $Q = 172 \pm 11$, $\omega = 214.7 \pm 0.2kHz$ and $\kappa = 2.32 \pm 0.21nN{\cdot}m$. The missing data between 215.3kHz and 215.6kHz was a noisy peak, so it was removed to help with fitting.

4.2 Calibration Factor

The calibration factors α, convert the vertical and lateral photodiode deflections into the cantilever deflections in nm as in equations 4.1 and 4.2.

4.2.1 Cantilever Tilt

The cantilever hangs on an angle θ from its substrate. The cantilever deflection is calibrated with respect to movement in the z-piezo which is strictly vertical and measures the quantity x_{Nvert} in figure 4.1. However, the actual deflection of the cantilever is perpendicular to the plane containing its length and width. Because the displacement from equilibrium is very small, we can assume that the angle is constant during deflection even though it is technically changing. Basic trigonometry applied to figure 4.1 then gives the relation for the actual deflection:

$$x_N = \frac{x_{Nvert}}{cos\theta} \tag{4.8}$$

For the ORC-B cantilever, $\theta = 12 \pm 1\,^{\circ}$, so x_{Nvert} needs an approximate 2% increase to get x_N.

4.2.2 Deflection Sensitivity

The deflection sensitivity is the quantity that converts the photodiode voltage into nm. This is generally straightforward for flexural deflection, but quite difficult for the lateral deflection because the lateral spring constant is much larger.

Flexural Deflection Sensitivity

If the cantilever is brought into a very hard surface that does not deform at all, the z-piezo displacement $z\{nm\}$ will equal the vertical deflection $x_{Nvert}\{V\}$. Their ratio is known as the deflection sensitivity s:

$$s = \frac{\Delta z\{nm\}}{x_{Nvert}\{V\}}$$

Once this has been obtained, the cantilever deflection during an experiment (even if the sample is soft) can be converted into nm.

Polymers are compressible, so the beaded cantilever cannot be used for deflection sensitivity calibration. A separate cantilever's deflection sensitivity s_{test} of the same type must instead be used to obtain the deflection sensitivity for the target cantilever s_{tar} with a linear adjustment for lever arm L' and photodiode intensity T (quantities defined in figure 4.1) by: [67]

$$s_{tar} = s_{test}\left(\frac{L'_{tar}}{L'_{test}}\right)\left(\frac{T_{test}}{T_{tar}}\right) \tag{4.9}$$

The deflection sensitivity should be linear. However, due to photodiode non-linearities, the deflection sensitivity becomes significantly larger at voltages greater than $|\pm 4V|$ as seen in the non-linear force distance curve and the plot of deflection sensitivity as a function of vertical deflection in figures 4.8 and 4.10 respectively.

To get the vertical deflection in any given force distance curve, it is not as simple as multiplying the deflection sensitivity at a certain voltage by that vertical deflection voltage because this assumes the deflection sensitivity was the same all throughout the deflection when it is in fact changing. To get the real vertical deflection, we need to sum over each change in deflection multiplied by the deflection sensitivity during that change. Since the deflection sensitivity is continuous, we can convert the summation into the integral:

$$x_b\left\{nm\right\} = \int_a^b s\left[x\left\{V\right\}\right]\,\mathrm{d}x\left\{V\right\} \tag{4.10}$$

The deflection sensitivity is a non-linear function of the vertical deflection voltage, and can be fit with a fourth order polynomial as in fig 4.10. The integration from a to b sums from an initial deflection a to a final deflection b. However, because the corrected deflection is actually linear, the deflection is relative, and we can calculate a deflection in nm corresponding to each deflection in V. During the experiment, the contact point deflection at point a will be subtracted from point b to get the absolute vertical deflection. This deflection $x_b\left\{nm\right\}$ is then:

$$x_b\left\{nm\right\} = \int \Big(Ax^4 + Bx^3 + Cx^2 + Dx + E\Big)\,\mathrm{d}x \tag{4.11}$$

Where x is the deflection in V and the constants A, B, C, D and E are from the equation for s and are given in figure 4.10. This gives the deflection in nm as a function of the deflection in V to be:

$$x_b\left\{nm\right\} = 0.001388x^5 - 0.000691x^4 + 0.00926x^3 - 0.0406x^2 + 68x \tag{4.12}$$

This equation corrects for the photodiode non-linearities during force distance curves as in the corrected force distance curve in figure 4.11.

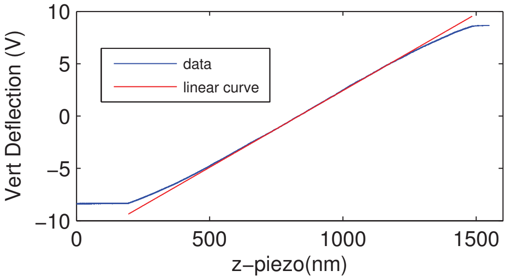

Figure 4.8: These data give the deflection per z-piezo movement for the test probe. The data are not linear because of photodiode non-linearities.

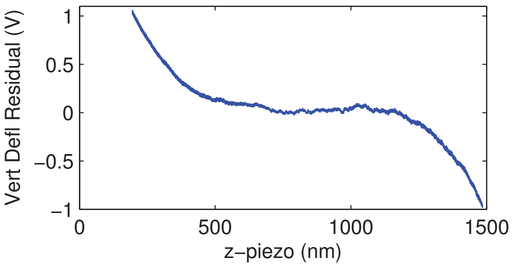

Figure 4.9: This is the residual of figure 4.8, with the linear curve subtracted from the non-linear data. Plotted to show the deviation from linearity.

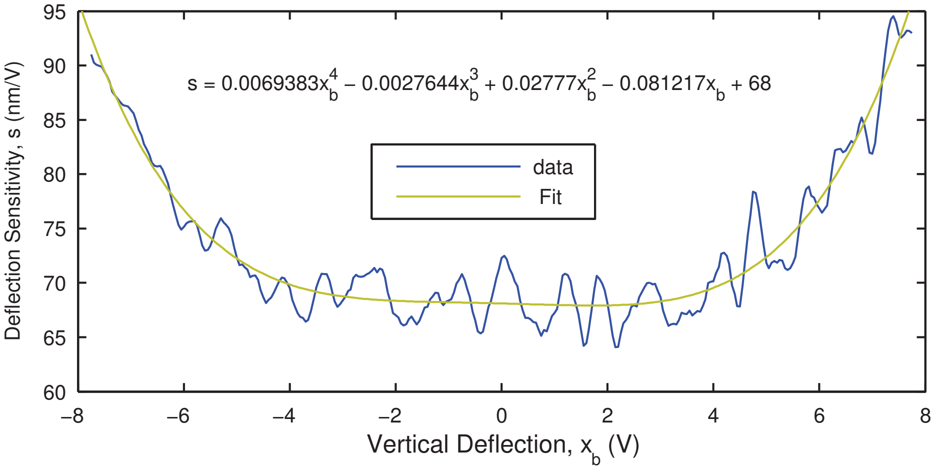

Figure 4.10: A plot of the deflection sensitivity as a function of the vertical deflection for the test probe. Obtained by taking the linear slope of small chunks that make up the curve in figure 4.8 and plotting them against the average vertical deflection of each chunk. The equation of the fitted curve is the variable $s\left[x\left\{V\right\}\right]$ in equation 4.10.

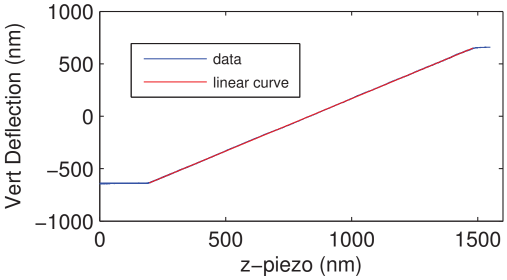

Figure 4.11: These are data converted to nm from figure 4.8, with the photodiode non-linearities corrected by using equation 4.12.

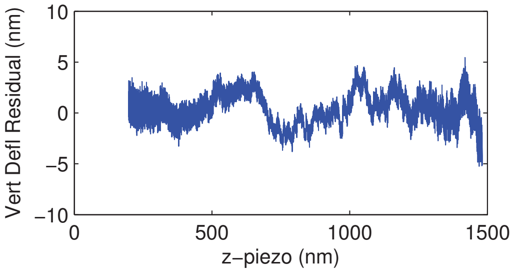

Figure 4.12: This is the residual of figure 4.11, with the linear curve subtracted from the linearised data. The only deviation from linearity is due to noise.

Lateral Deflection Sensitivity

Lateral deflection sensitivity determination is much harder because the lateral spring constant k_L is about 1000 times larger than the normal spring constant and can be comparable to the lateral in-plane bending stiffness k_{IPL}. The effective lateral spring constant is $k_{EffL}^{-1} = k_L^{-1} + k_{IPL}^{-1} + k_{ContL}^{-1}$ where k_{ContL} is the lateral contact stiffness. This means that the sticking portion of each friction loop cannot be used for calibration because the normal spring constant is comparable to the lateral in-plane bending stiffness for our cantilever. The deflection sensitivity is instead measured by using the test probe method by Cannara et al. [67]

To perform the test probe method, a large bead is glued to the cantilever to decrease the lateral spring constant so that it is much smaller than the in-plane and contact spring constants. This means that $k_{EffL} \approx k_L$. Ensuring that this is true means showing that $\frac{k_L}{k_{IPL}} \ll 1$. Sader and Green have shown that given the lateral and normal spring constants, this ratio ϵ_{test} can be determined by: [69]

$$\epsilon_{test} = \frac{k_L}{k_{IPL}} = \frac{\kappa}{k_N}\frac{t}{hw}^{2}\frac{L'}{L}^{2} \tag{4.13}$$

Similarly to the vertical deflection sensitivity, displacing the test probe cantilever laterally by $y\,\{nm\}$ into an very hard surface will give a horizontal deflection $x_T\,\{V\}$. Their ratio gives the test probe lateral deflection sensitivity $s_{lat,test}$. As in the vertical deflection sensitivity, an adjustment between test and target probe lever arms (here, the lever arms are the height from the cantilever neutral axis to contact) and between photodiode intensities is needed. Another adjustment to account for in-plane bending between target and test probe is also needed. These adjustments give the target probe lateral deflection sensitivity $s_{lat,tar}$:

$$s_{lat,tar} = s_{lat,test}\left(\frac{h_{tar}}{h_{test}}\right)\left(\frac{T_{test}}{T_{tar}}\right)\left(\frac{1+\epsilon_{tar}}{1+\epsilon_{test}}\right) \tag{4.14}$$

where ϵ_{test} is virtually negligible, but ϵ_{tar} is not. GaAs was used as a calibration sample because it is a rigid body and because it cleaves at a perfect 90° angle. A 60μm bead is glued onto a test probe, and pushed perpendicularly into the cleaved vertical GaAs surface as depicted in figure 4.13.

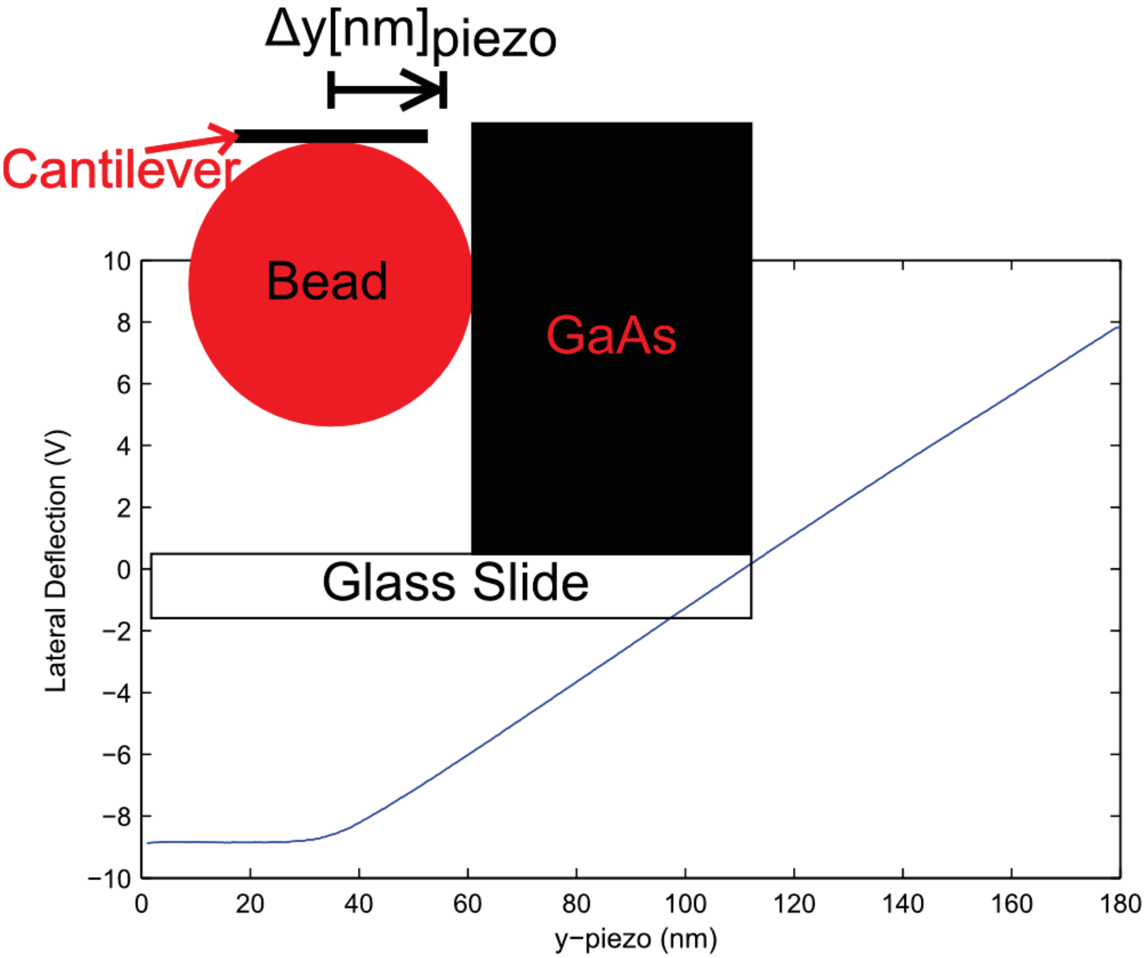

Figure 4.13: Analogous to figure 4.8 but laterally, this curve gives the lateral deflection per y-piezo movement for the test probe. The figure also shows the experimental set-up for this measurement.

Lateral photodiode non-linearities are corrected in the same way as those in the vertical signal. The correction is usually less important because the lateral signal in this experiment does not typically use the full photodiode range. However, the photodiode non-linearities are still corrected. This is done by integrating over the lateral deflection sensitivity as a function of lateral deflection $x_L \{V\}$ (obtained from figure 4.14) times by a variation in lateral deflection to get a lateral deflection in nm $x_{L,b} \{nm\}$:

$$x_{L,b} \{nm\} = 0.000034x_L^5 + 0.000228x_L^4 + 0.00163x_L^3 + 0.0195x_L^2 + 7.6x_L \qquad (4.15)$$

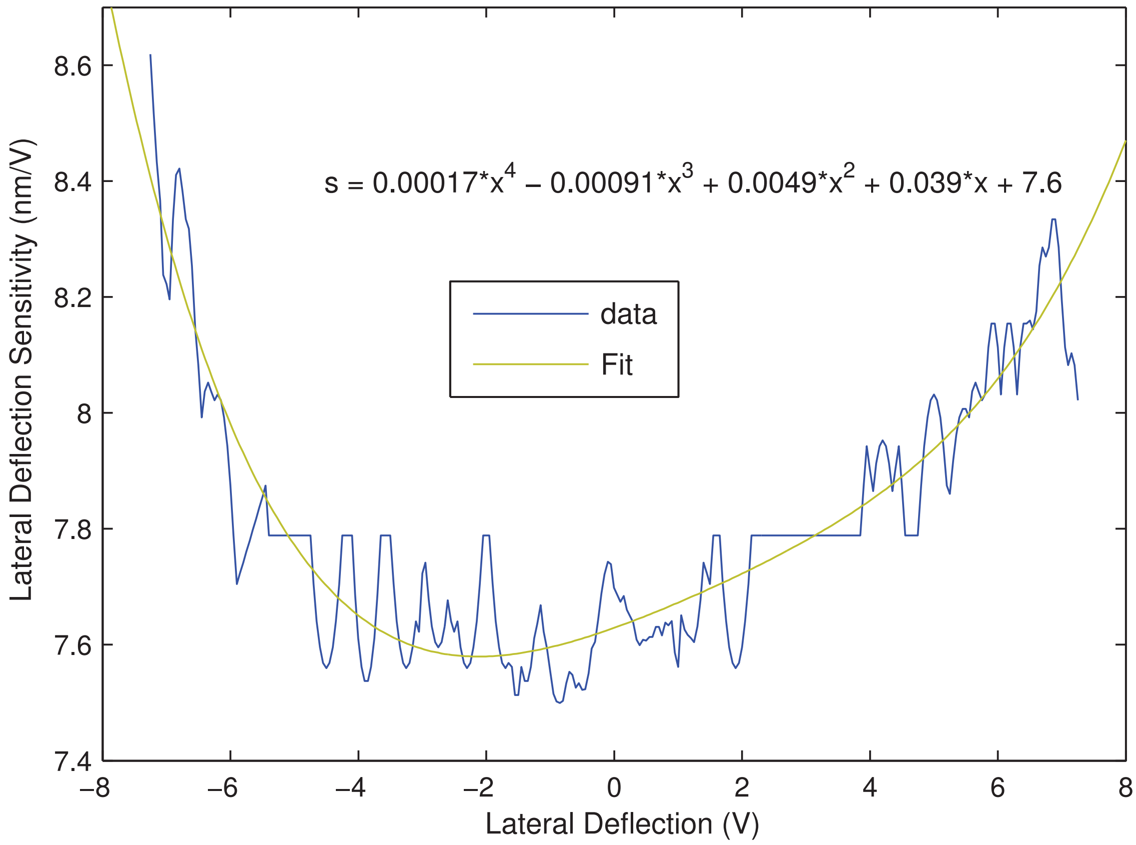

Figure 4.14: Analogous to figure 4.10 but laterally, this curve gives the lateral deflection sensitivity as a function of lateral deflection obtained from figure 4.13. The equation of the fitted curve is used to obtain equation 4.15.

4.3 Tracking Lens Error

In Chapter 3.2.3, the tracking lens error due to the crack in the z-piezo is shown to be approximately linear with the y-piezo scanner movement. It is thus a systematic error that can be subtracted from the data. A sawtooth function is fit to the tracking lens error and subtracted from the friction force distance curve data using Matlab as shown in fig4.15. The fit is performed on the data before the cantilever comes into contact with the surface. The purpose of this fit is to obtain the phase shift and amplitude of the error. The frequency of oscillations is known because all time dependence of the scan is input by the user. If the frequency from the fitted curve is used, it can be slightly incorrect, leading to very large errors as in figure 4.17 compared to 4.16. An incorrect frequency is so dangerous because it increases the friction as the normal load increases, so it can go undetected. Further confusing the problen is that the reported software value used to calculate the frequency is not precise to enough significant figures unless the value is obtained by looking inside the data file's header.

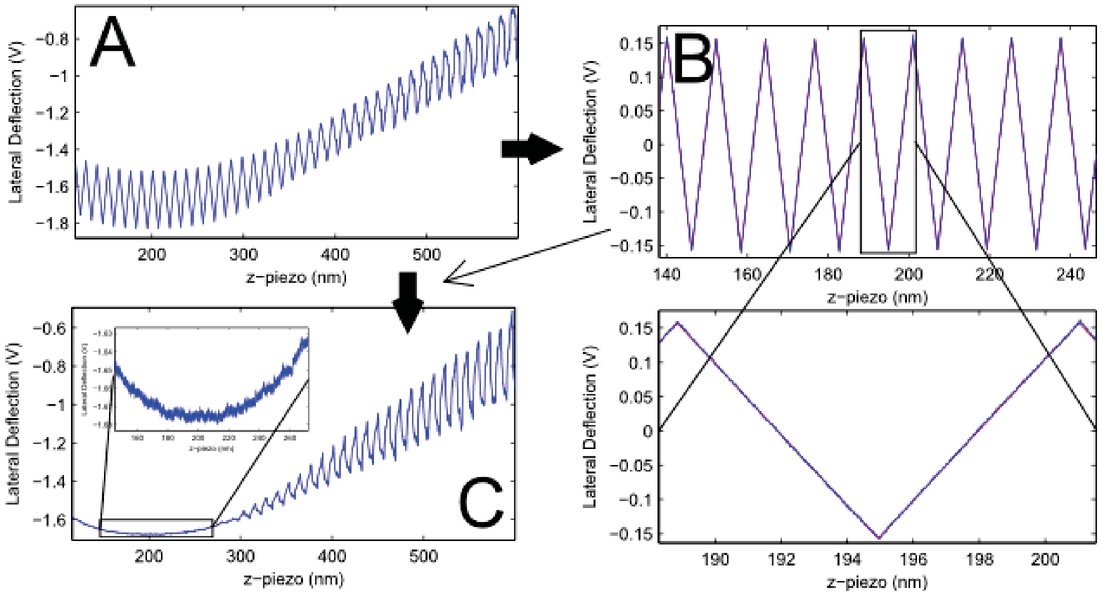

Figure 4.15:
A. Raw data of a lateral deflection distance curve (clearly the tracking lens error is obfuscating the friction signal).
B. Lateral deflection from **A** before the probe comes into contact with the sample, fitted with a sawtooth function (and flattened to be able to fit).
C. The sawtooth function obtained in B subtracted from the lateral deflection distance curve in **A**. This is the friction signal with the tracking lens error subtracted.

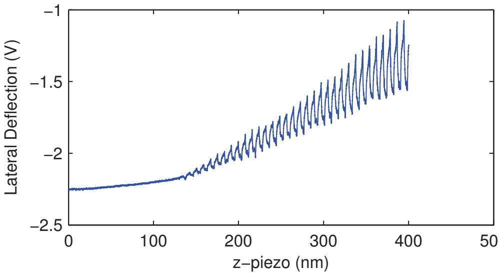

Figure 4.16: This is a lateral deflection distance curve after having the tracking lens error subtracted.

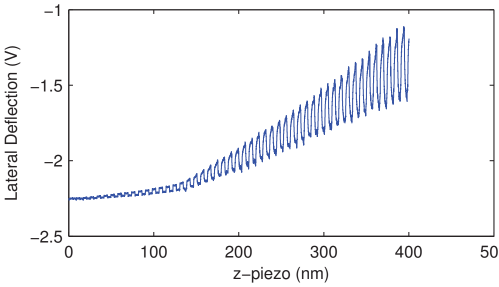

Figure 4.17: As in figure 4.16, this is the lateral deflection signal after having the tracking lens error subtracted. However, here, the tracking lens sawtooth fit frequency has a tiny error of 0.4%.

4.4 Data Analysis

A Matlab program was written in order to analyse the data from this new friction force distance curve microscopy. The raw data consists of the lateral and vertical deflections as a function of the z-piezo movement. Here are the general steps contained in the Matlab code in order to obtain a graph of friction force vs. normal force:

1. The tracking lens error is fit with a sawtooth function and is then subtracted from the lateral deflection data.
2. The lateral deflection data is then converted into a friction force. This is achieved by:
    (a) Multiplying the data by the lateral calibration factor and spring constant.
    (b) Choosing points for positive and negative lateral deflections in the friction force distance curve, subtracting them from each other and then dividing by 2 (friction torques the cantilever in both scan directions, so the signal needs to be divided by 2).
3. The vertical deflection data is converted into a normal force. This is achieved by:
    (a) Multiplying the data by the vertical calibration factor and the normal spring constant.

   (b) Choosing the contact point in the data to obtain absolute normal forces.
   (c) Fitting the virtual deflection and subtracting its slope from the data.
4. Matching friction and normal force data points up according to z-piezo position.
5. Plotting the friction force against the normal force to obtain a kinetic friction coefficient.

4.5 Summary

The calibration steps in this chapter allow the conversion of the lateral and vertical deflection signals in V to be converted into the friction and normal forces in nN respectively. The full expressions in terms of quantities defined in this chapter are:

$$F_N = \frac{k_N}{cos\theta}\left(\frac{L_{tar}}{L'_{tar}}\right)^3 s_{N,test}\left[x_N\left\{V\right\}\right]\left(\frac{L'_{tar}}{L'_{test}}\right)\left(\frac{T_{test}}{T_{tar}}\right)x_N\left\{V\right\} \tag{4.16}$$

$$F_L = \frac{k_L}{h_{tar}^2}\left(\frac{L_{tar}}{L'_{tar}}\right)s_{L,test}\left[x_L\left\{V\right\}\right]\left(\frac{h_{tar}}{h_{test}}\right)\left(\frac{T_{test}}{T_{tar}}\right)\left(\frac{1+\epsilon_{tar}}{1+\epsilon_{test}}\right)x_L\left\{V\right\} \tag{4.17}$$

5

Results

5.1 Force Distance Curves

5.1.1 Force Compression Curves

When the cantilever extends into a very hard surface, the deflection equals the z-piezo extension, and their ratio gives the deflection sensitivity. However, during the experiment, there are compressible polymers on both the bead and on the sample. This means that some of the z-piezo extension during the experiment isn't converted into cantilever deflection, but into polymer compression as in figure 5.1. The deflection sensitivity during the experiment $s_{N,exp}$ should always be smaller than or equal to the target deflection sensitivity $s_{N,tar}$ by the relation:

$$s_{N,tar} = s_{N,test}\left(\frac{L_{tar}}{L_{test}}\right)\left(\frac{T_{test}}{T_{tar}}\right) \geqslant s_{N,exp} \tag{5.1}$$

This provides a quick check to make sure the calibration is consistent. Another important feature of this equation is that $s_{N,tar} = s_{N,exp}$ only if there is no compression. In the polymer friction experiment, this condition means that the polymers have been completely compressed and there is now hard repulsion between silica surfaces (known as hitting the hard wall). The amount of compression c can be calculated as the amount of z-piezo extension z that is not converted into a deflection x by the cantilever:

$$c = z - x \tag{5.2}$$

This allows comparison of compression curves to the friction vs normal force curves. Also, by taking a force compression curve before the experiment,

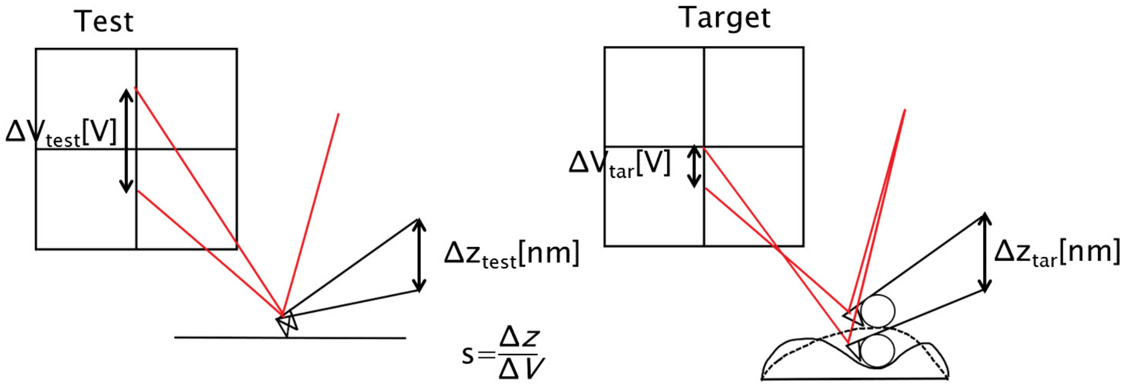

Figure 5.1: Difference in deflection sensitivity when compressing soft and hard samples.

one can obtain the optimal amount of force to apply during a friction force distance curve without completely compressing the polymers and risking damaging them. Force compression curves below and above the pKa of about pH 8.7 are presented in figures 5.2 and 5.3 respectively.

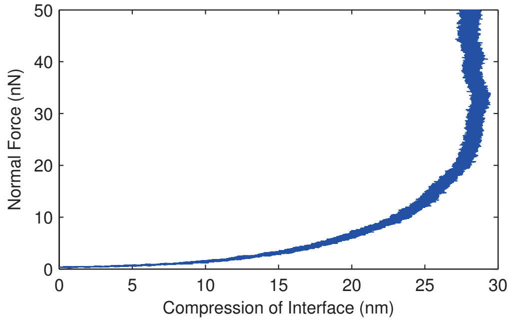

Figure 5.2: Force compression curve in pH 7.5 solution (below the pKa). Hits the hard wall at about 20nN normal force and 28nm compression.

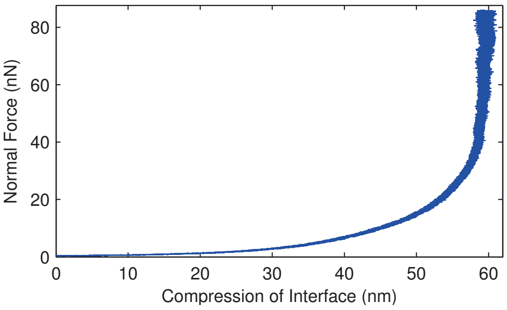

Figure 5.3: Force compression curve in pH 9.5 solution (above the pKa). Hits the hard wall at about 35nN normal force and 58nm compression.

The zero point in these curves was defined as the point where the cantilever jumped into contact and was subsequently deflected. This was sometimes hard to define, and introduced between 2-5nm uncertainty in compression measurements. Most force compression curves hit the hard wall between 20-35nN, so experiments that far exceed these normal forces should be avoided. These force compression curves also give an estimation of the thickness of the polymer layers at different pH values, shown in table 5.1. As expected, polymer layers appear thicker for pH values above the pKa of pH 8.7 (here by about 2 times). All of the measurements appear to be about three times smaller than in Borozenko's measurements using ellipsometry. It could be that our measurements are underestimated and that the hard wall doesn't represent silica-on-silica pressure, but instead the polymer being compressed to a point where it becomes rigid. At the very least, these measurements give a lower bound on the polymer thickness. The uncertainty on these measurements was estimated by combining the uncertainty arising from the zero point determination, hard wall determination, the error from the calibration factor (see section 5.2.1) and the standard deviation between multiple curves.

	Compression (nm)	Retraction (nm)	Ellipsometry (nm)
Water	15 ± 15	152 ± 22	41 ± 11
pH 7.5	14 ± 10	146 ± 30	45 ± 8
pH 8.5	17 ± 14	155 ± 35	54 ± 7
pH 9.5	30 ± 14	130 ± 21	82 ± 10
pH 10.5	33 ± 12	137 ± 20	93 ± 8

Table 5.1: Polymer thicknesses for the second beaded experiments in unsalty solution using compression curves, retraction curves and ellipsometry (by Borozenko). [58]

5.1.2 Long-Range Polymer Adhesion

During retraction of the bead from the surface, the deflection will usually follow approximately the same shape as in the extension except with some hysteresis because the polymers are viscoelastic (see figure 2.7 for hysteresis in force distance curves). However, because the polymers can intertwine, the polymerized bead can adhere very strongly to the polymerized surface. This can be seen by a series of small jumps as the bead comes away from the surface in figure 5.4. The source of the jumps is likely polymer disentanglement and the space in between jumps, structural transitions of the polymer. The polymers are not being ripped off the surface because this would be indicated by an adhesive force that continues to increase until one final big jump (larger than all the rest) out of contact. This is because the last jump needs to be the disconnection between adhering polymers, but the strength of the disconnecting force must also be greater than all the other jumps because otherwise they would have simply disconnected at one of those previous points.

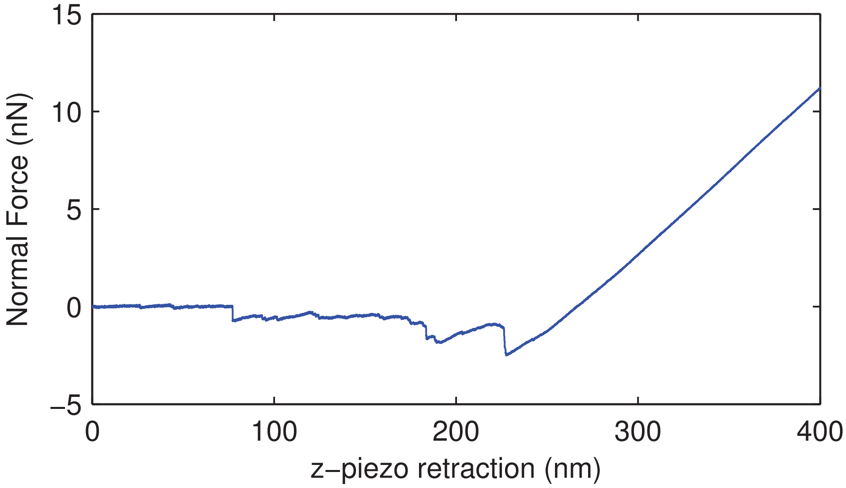

Figure 5.4: Long-range polymer adhesion between PS-PAA polymers. Both disentanglement and structural transitions of the polymer can be seen by jumps and the space between jumps during adhesive contact (when the force is below 0nN).

As with the compression measurements, these polymer extension curves (the retraction part of a force distance curve) can provide further information on the polymer length. For these curves, the polymer length is measured as the z-piezo retraction from when the force becomes negative (the cantilever is held in contact with the surface only due to adhesion) to the moment when there are zero forces applied to the cantilever (the cantilever jumps up as the restoring force overcomes the polymer adhesion force and the polymer layers separate). The uncertainty on these measurements was estimated by combining the uncertainty arising from the zero point determination, separation point determination, the error from the calibration factor (see section 5.2.1) and the standard deviation between multiple curves. For a correct measurement, the cantilever deflection for the last jump must be subtracted because the polymers have already reached their full extension. After dividing by 2 accounting for the fact that there are two polymer layers involved, the polymer lengths measured with this method are still longer than those measured by ellipsometry (see table 5.1). This is expected because the polymer is being stretched beyond its normal configuration by a force equal to the adhesion force. The polymer lengths for all pHs were equal within error because swelling doesn't affect the physical length of the polymers. The overestimation in pulling and underestimation in compression give upper and lower bounds on the polymer lengths. These polymer extension curves also confirm that polymers are not being ripped off of the surface during the experiment because a single layer of polymers would not exhibit this behaviour.

5.2 Friction Measurements and Discussion

5.2.1 Friction Measurements

Friction force distance curve microscopy was performed on two beaded cantilevers to obtain the kinetic friction coefficients in water and salt solutions over a wide range of pH values, presented in table 5.2. It is interesting to note while looking at table 5.2 that, in other literature, polymer brush systems claiming to have very low friction coefficients have coefficients on the order of 10^{-3}. [59,60,71] These were observed using both surface force apparatus and beaded AFM measurements.

	Cantilever 1		Cantilever 2	
pH	Non-Salty μ_k	Salty μ_k	Non-Salty μ_k	Salty μ_k
Water	0.3 ± 0.1	0.36 ± 0.13	0.51 ± 0.09	0.28 ± 0.14
7.5	0.31 ± 0.06	0.18 ± 0.08	0.17 ± 0.1	0.14 ± 0.09
8.5	0.35 ± 0.06	N/A*	0.06 ± 0.06	0.26 ± 0.14
9.5	0.14 ± 0.12	0.27 ± 0.09	0.16 ± 0.08	0.055 ± 0.035
10.5	0.19 ± 0.1	0.12 ± 0.10	0.26 ± 0.18	0.16 ± 0.1

Table 5.2: Kinetic friction coefficients
*No coefficient of friction available because of time limitations.

The friction coefficients reported are mean values from multiple individual friction measurements. The estimated uncertainty for the reported values was obtained by calculating the standard deviation of the set of measurements and combining it with the error associated to each measurement. For each measurement, the method of least squares was used to estimate the uncertainty of the slope in plots of friction force versus normal force. Associated to both the normal force and the frictional force are uncertainties of about 5% and 13% respectively. These quantities are expressed in terms of the calibration factors and spring constants in equations 4.2 and 4.1. The normal and lateral spring constants have been calculated to have about 3.7% and 7.8% uncertainty. The main contributions to the normal spring constant uncertainty was from the quality factor and cantilever width, which both had 2% errors on their measurements. The only major contribution to the lateral spring constant uncertainty was the lateral quality factor, which had about 7% error on its measurement. The normal and lateral calibration factors have been calculated to have about 4% and 8% errors. The only major contribution to the normal calibration factor uncertainty was from the vertical deflection sensitivity, which had about 4.5% error on its measurement. The most significant contributions to the lateral calibration factor uncertainty was from the lateral deflection sensitivity and from the in-plane bending correction, which had about 4% and 6% error on their measurements respectively. The 5% and 13% errors on the normal and frictional forces, combined with 'end friction' (discussed in section 5.2.2) and a large amount of variation between measurements has yielded friction coefficient uncertainties of up to 100% (17% was the smallest percent uncertainty).

Given the uncorrelated variation in kinetic friction values and the amount of error associated to each one, there appears to be no friction dependence on pH value or salt concentration. It is unclear whether this non-dependence is due to a problem with the experiment or there truly is no dependence.

5.2.2 Friction Discussion

In certain friction force distance curves, there appear to be dramatic increases in friction at the end of each friction loop with respect to the rest of the loop (here called 'end friction'). This is shown in figure 5.5. The end friction from loop to loop appears to increase with normal force. To eliminate the effect of this end friction, one might think of measuring the friction from the midpoint in each loop. Unfortunately, even taking these midpoints for the friction measurement causes an overall increase in the friction coefficient compared to when their is no end friction evident. This effect is most obvious in the friction loop in figure 5.6 where the end friction appears to start halfway through the friction force distance curve, and the friction coefficient increases at the same moment in figure 5.7. This is a unique case as the end friction is usually either present or absent. The end friction appears to be a large source for the variation in friction curves, and could be the reason for which no dependence is observed. It is possible that the experiment, analysis or instrumentation are somehow flawed. The end friction could be a result of this flaw, or it could be an interesting polymer-polymer interaction.

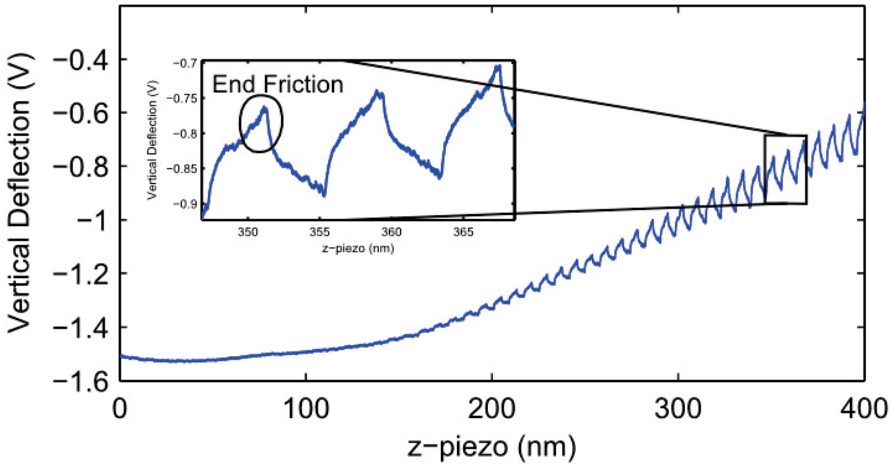

Figure 5.5: A typical friction force distance curve with 'end friction'.

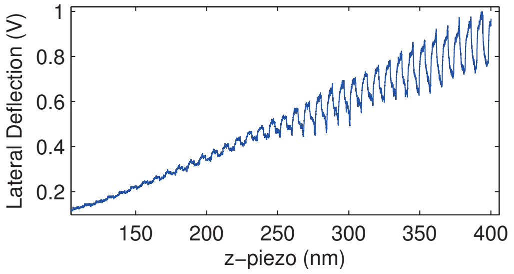

Figure 5.6: The lateral deflection for a friction force distance curve. End friction starts halfway through the curve.

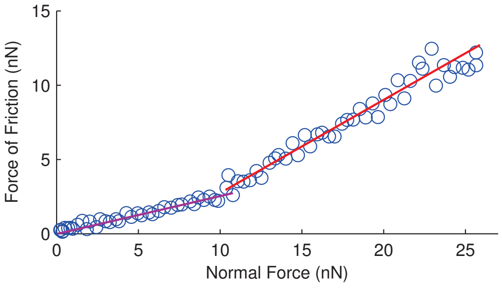

Figure 5.7: Friction vs normal load from the measurement in figure 5.6. The friction coefficient goes from 0.24 to 0.61 when the end friction starts.

Experiment Verification

It might be proposed that the crack in the piezo or some hardware/instrumentation problem is the issue. The tracking lens error due to the piezo crack in combination with in-plane bending was analysed. During each scan, the tracking lens error is reduced by in-plane bending, but it is corrected for as though it isn't reduced. Because of this, the friction signal is smaller than it should be, but only by a negligible 0.03% correction. To test the hardware, friction measurements for a silicon nitride tip on a GaAs surface were obtained and are shown in figure 5.8. They do not display any end friction in their scope traces. This indicates that the instrument itself is not the source of the end friction.

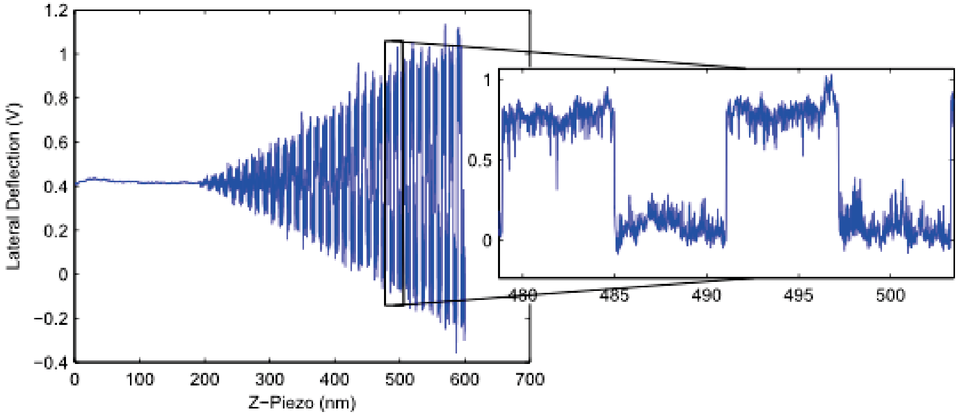

Figure 5.8: Friction force distance curve of a silicon nitride tip on a GaAs surface. Zooming in on the individual friction scan scope trace, it can be seen that there is no end friction present in these scans.

Friction measurements for a silicon nitride tip on GaAs and a polymerized bead on a polymerized surface were obtained using FFDCM and STFFM to see if the new method was the issue. Both methods and experiments yielded the same friction coefficient as seen in figures 5.10 and 5.11, even though the beaded experiment (figure 5.11) displayed end friction as seen in figure 5.9. This means that the new method is not the source of the end friction.

During beading, the beads were not glued perfectly on the neutral axis of the cantilever. Their displacement from the neutral axis d, was $d = 1.0 \pm 0.5\mu m$ and $d = 0.5 \pm 0.5\mu m$. For lateral forces, the cantilever's axis of rotation shifts from the

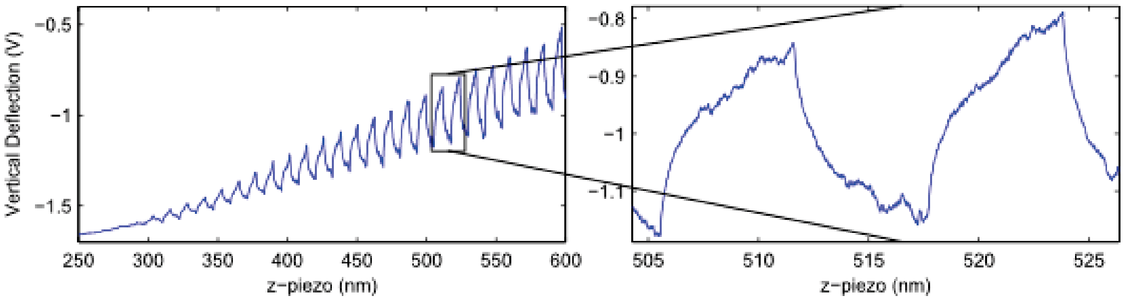

Figure 5.9: Friction force distance curve of a polymerized bead on polymerized surface in water. By zooming in on individual friction scan scope traces, it can be seen that end friction is present. Both methods' friction coefficients for this measurement are the same (as seen in figures 5.10 and 5.11) despite end friction being present.

neutral axis. This does not change the rotational spring constant or lever arm, so the friction measurement is unaffected. However, for normal forces, the cantilever will now be torqued with a lever arm d. The cantilever will thus feel a force in torsional and flexural modes and must be modelled as two springs in series. The cantilever's effective spring constant for normal forces thus changes. The corrections to the normal force measurement and to the frictional force measurement due to this change are fortunately negligible at about 0.02% and 0.00005% respectively (for a bead displacement of $d = 1.5\mu m$).

Polymer Interactions

The previous section's results indicate that the approach and method are not flawed, and that the crack in the piezo and the presence of the bead have no obfuscating effects on the friction measurements. It is more likely then that the results can be better explained by polymer-polymer interactions.

The end friction could be caused by polymers being shovelled to one side during a scan. With an accumulation of polymers to the sides, there would be more lateral resistance at the ends of each scan. The end friction would increase as more polymers accumulate, and thus with the normal force. It could be that this only happens in some curves because different polymer regions resist wear differently. Similarly, another possible explanation for the end friction is that the polymers are being parted and then squished sideways. Here again, an accumulation of polymers to one side could cause an increase in friction and different regions on the sample might not allow the parting to occur. With both of these theories, the polymers would probably be forced more to one side than the other, giving rise to an asymmetry in end friction between scan directions. Asymmetries have been observed in both scan directions. See figures 5.12 and 5.13 for measurements displaying end friction in the same experimental conditions.

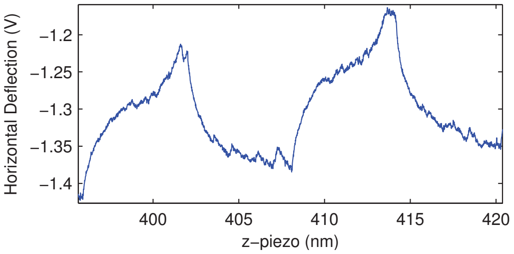

Figure 5.12: The end friction here is in the positive y-piezo scan direction.

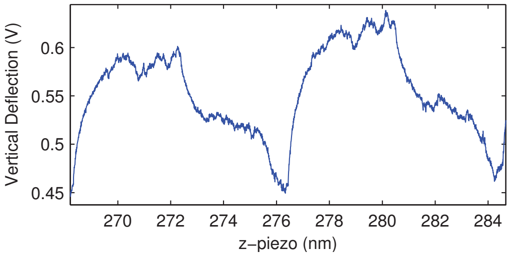

Figure 5.13: The end friction here is in the negative y-piezo scan direction.

It could also be that this is simply a characteristic of sliding over these polymers. For example, there could be some adhesion between polymers during lateral scans such that the maximum friction happens at each friction loop end. Given that the size of scan used was usually 340nm, and we have seen that the long range adhesion force can act over about 300nm, the increase in lateral adhesion would likely be maximized towards the end of the scan when the largest number of polymers has been contacted. The lateral adhesion would also increase with normal load as more polymers intertwine.

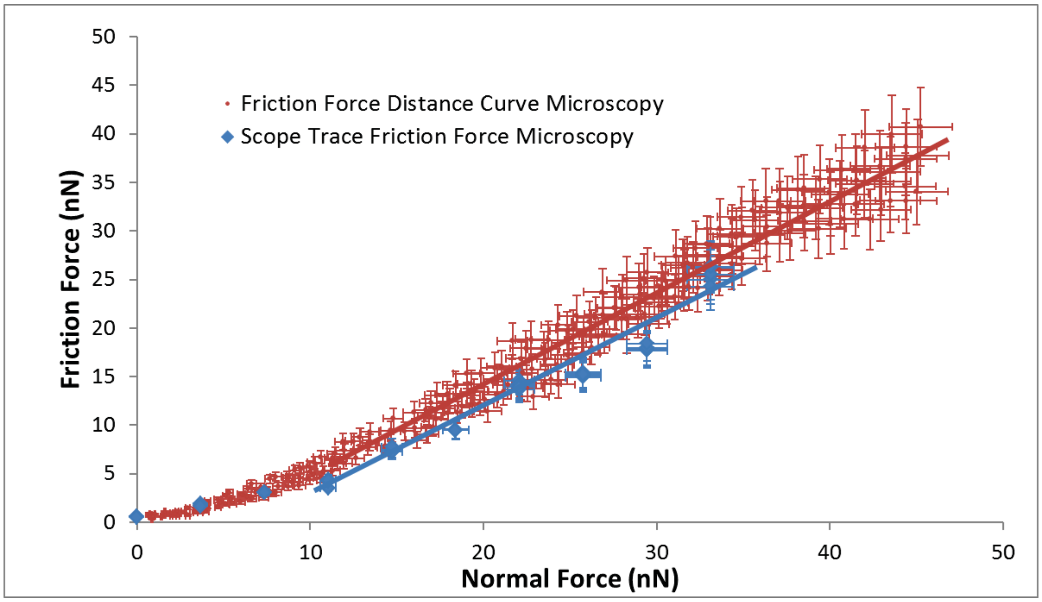

Figure 5.10: The friction force plotted as a function of the normal force for a silicon nitride tip on a GaAs surface in water. The friction coefficient using FFDCM and STFFM are 0.91±0.21 and 0.88±0.18 respectively. Both methods agree within error.

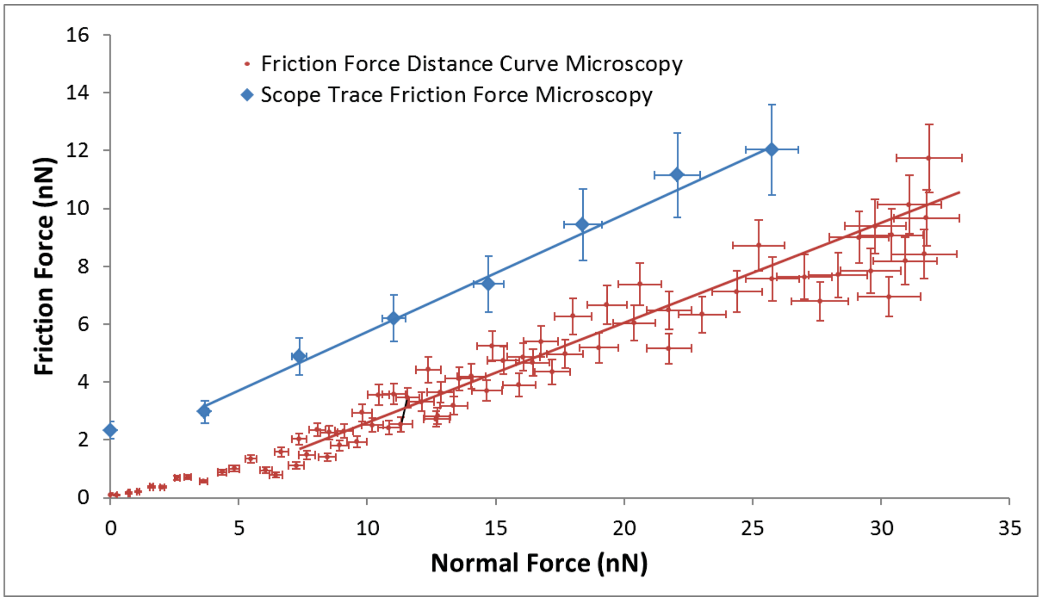

Figure 5.11: The friction force plotted as a function of the normal force for a polymerized bead on a GaAs surface in water corresponding to data in figure 5.9. The friction coefficient using FFDCM and STFFM are 0.35±0.12 and 0.4±0.1 respectively. Both methods agree within error.

5.3 Conclusions and Future Research

I have developed a new method for AFM friction force measurements called friction force distance curve microscopy (FFDCM). It has been compared to the standard method for measuring friction using an AFM, and both methods yield the same results within error. I have also made absolute friction measurements through a lengthy calibration procedure. In order to show that this new method is accurate, surfaces with known friction coefficients can be measured using FFDCM to verify that absolute measurements are correct.

The tracking lens systematic error was eliminated from the data for these measurements. It can henceforth be used as a heuristic where periodic signals in AFM are suspected as the cause of a systematic error. Taking the Fourier transform of all data is regular practice to identify systematic error through periodicity, but this is especially important for AFM experiments because lateral probing is almost always, and vertical probing is often, periodic.

Though there is some variation in friction between pH and salt conditions, there is no negative correlation between the swelling of these polymer brushes and the friction coefficient. The end friction found in this study is an interesting polymer-polymer interaction which can be further studied. If the mechanism causing end friction can be identified, it could be eliminated or its effect neutralized in future polymer brush designs. The size of the scan can be increased to test the hypothesis that end friction is caused by increases in the lateral adhesion over small distances.

A

Bioscope Alternate Configuration Signals

When the Bioscope is in the alternate configuration, the signals accessible through the signal access module (SAM) are different from those in the standard configuration, and are not noted in the manual. The SAM Analog Inputs to NanoScope ±10VDC in the alternate configuration were identified and are presented in table A.1 below for future reference.

Lines	**Tapping Mode Signal (Volts)**	**Contact AFM Signal (Volts)**
In 0	Vertical deflection minus setpoint voltage	(Vertical deflection minus setpoint voltage)*1.25
Aux A	Lateral deflection (LFM)	Lateral Deflection (LFM)
Aux B	Vertical deflection	Vertical deflection
Aux C	Photodiode array sum (A+B+C+D)	Photodiode array sum (A+B+C+D)

Table A.1: These are the Signal Access Module Analog Inputs to NanoScope ±10VDC when the Bioscope is in the alternate configuration.

Bibliography

[1] Horst Czichos. *Tribology: a systems approach to the science and technology of friction, lubrication, and wear*, volume 1. Access Online via Elsevier, 2009.

[2] John H Dumbleton. *Tribology of natural and artificial joints*, volume 3. Elsevier, 1981.

[3] John Williams. *Engineering tribology*, volume 10. Cambridge University Press, 2005.

[4] Duncan Dowson and Duncan Dowson. *History of tribology*. Longman London, 1979.

[5] C.A. Coulomb. *Theorie des machines simples: en ayant egard au frottement de leurs parties et a la roideur des cordages*. Bachelier, 1821.

[6] GA Tomlinson. Cvi. a molecular theory of friction. *The London, Edinburgh, and Dublin philosophical magazine and journal of science*, 7(46):905–939, 1929.

[7] E Gnecco, R Bennewitz, T Gyalog, and E Meyer. Friction experiments on the nanometre scale. *Journal of Physics: Condensed Matter*, 13(31):R619, 2001.

[8] Frank Philip Bowden and David Tabor. *The friction and lubrication of solids*, volume 1. Oxford university press, 2001.

[9] Jianping Gao, WD Luedtke, D Gourdon, M Ruths, JN Israelachvili, and Uzi Landman. Frictional forces and amontons' law: from the molecular to the macroscopic scale. *The Journal of Physical Chemistry B*, 108(11):3410–3425, 2004.

[10] Robert W Carpick, D Frank Ogletree, and Miquel Salmeron. A general equation for fitting contact area and friction vs load measurements. *Journal of colloid and interface science*, 211(2):395–400, 1999.

[11] KL Johnson, K Kendall, and AD Roberts. Surface energy and the contact of elastic solids. *Proceedings of the Royal Society of London. A. Mathematical and Physical Sciences*, 324(1558):301–313, 1971.

[12] BV Derjaguin, VM Muller, and Yu P Toporov. Effect of contact deformations on the adhesion of particles. *Journal of Colloid and interface science*, 53(2):314–326, 1975.

[13] Daniel Maugis. Adhesion of spheres: the jkr-dmt transition using a dugdale model. *Journal of Colloid and Interface Science*, 150(1):243–269, 1992.

[14] Binquan Luan and Mark O Robbins. The breakdown of continuum models for mechanical contacts. *Nature*, 435(7044):929–932, 2005.

[15] W. Zhong and D. Tomanek. First-principles theory of atomic-scale friction. *Phys. Rev. Lett.*, 64:3054–3057, Jun 1990.

[16] Motohisa Hirano, Kazumasa Shinjo, Reizo Kaneko, and Yoshitada Murata. Observation of superlubricity by scanning tunneling microscopy. *Phys. Rev. Lett.*, 78:1448–1451, Feb 1997.

[17] Bharat Bhushan, Jacob N Israelachvili, and Uzi Landman. Nanotribology: friction, wear and lubrication at the atomic scale. *Nature*, 374(6523):607–616, 1995.

[18] J Krim, DH Solina, and R Chiarello. Nanotribology of a kr monolayer: A quartz-crystal microbalance study of atomic-scale friction. *Physical review letters*, 66(2):181–184, 1991.

[19] Gerd Binnig, Calvin F Quate, and Ch Gerber. Atomic force microscope. *Physical review letters*, 56(9):930, 1986.

[20] Ro Erlandsson, G Hadziioannou, C Mathew Mate, GM McClelland, and S Chiang. Atomic scale friction between the muscovite mica cleavage plane and a tungsten tip. *The Journal of chemical physics*, 89:5190, 1988.

[21] Robert W Carpick, N Agrait, DF Ogletree, and Miguel Salmeron. Measurement of interfacial shear (friction) with an ultrahigh vacuum atomic force microscope. *Journal of Vacuum Science & Technology B: Microelectronics and Nanometer Structures*, 14(2):1289–1295, 1996.

[22] NK Myshkin, MI Petrokovets, and AV Kovalev. Tribology of polymers: adhesion, friction, wear, and mass-transfer. *Tribology International*, 38(11):910–921, 2006.

[23] Jacob N Israelachvili and Patricia M McGuiggan. Forces between surfaces in liquids. *Science*, 241(4867):795–800, 1988.

[24] L. Bruschi and G. Mistura. Measurement of the friction of thin films by means of a quartz microbalance in the presence of a finite vapor pressure. *Phys. Rev. B*, 63:235411, May 2001.

[25] Lv Jizu, Bai Minli, Cui Wenzheng, and Li Xiaojie. The molecular dynamic simulation on impact and friction characters of nanofluids with many nanoparticles system.

[26] Uzi Landman, RN Barnett, and WD Luedtke. Simulations of materials: from electrons to friction. *Philosophical Transactions of the Royal Society of London. Series A: Physical and Engineering Sciences*, 341(1661):337–350, 1992.

[27] Otis R Walton. Numerical simulation of inelastic, frictional particle-particle interactions, 1993.

[28] P. Blau, P.J. Blau, and R.G. Bayer. *Wear of Materials*. Wear of Materials: Proceedings of the Fourteenth International Conference on Wear of Materials, Washington, DC, USA, 30 March-3 April 2003. Elsevier, 2003.

[29] D.R. Peterson and J.D. Bronzino. *Biomechanics: Principles and Applications, Second Edition*. Taylor & Francis, 2007.

[30] Hisae Yoshizawa, You Lung Chen, and Jacob Israelachvili. Fundamental mechanisms of interfacial friction. 1. relation between adhesion and friction. *The Journal of Physical Chemistry*, 97(16):4128–4140, 1993.

[31] GA Ateshian, VC Mow, and R Huiskes. Friction, lubrication, and wear of articular cartilage and diarthrodial joints. *Basic orthopaedic biomechanics and mechano-biology. 3rd ed. Philadelphia: Lippincott Williams & Wilkins*, pages 447–94, 2005.

[32] David A Swann, Kurt J Bloch, David Swindell, and Elizabeth Shore. The lubricating activity of human synovial fluids. *Arthritis & Rheumatism*, 27(5):552–556, 1984.

[33] Qing Zhang and Lynden A Archer. Step-growth synthesis and interfacial friction properties of surface dendron coatings. *Langmuir*, 22(2):717–722, 2006.

[34] MC LeMieux, S Peleshanko, KD Anderson, and VV Tsukruk. Adaptive nanomechanical response of stratified polymer brush structures. *Langmuir*, 23(1):265–273, 2007.

[35] Suk-kyun Ahn, Rajeswari M Kasi, Seong-Cheol Kim, Nitin Sharma, and Yuxiang Zhou. Stimuli-responsive polymer gels. *Soft Matter*, 4(6):1151–1157, 2008.

[36] Mikhail Motornov, Roman Sheparovych, Ihor Tokarev, Yuri Roiter, and Sergiy Minko. Nonwettable thin films from hybrid polymer brushes can be hydrophilic. *Langmuir*, 23(1):13–19, 2007.

[37] Flory and P J. *Principles of polymer chemistry*. Cornell University Press, 1953.

[38] Pierre Gilles De Gennes. *Scaling concepts in polymer physics*. Cornell university press, 1979.

[39] PG De Gennes. Scaling theory of polymer adsorption. *Journal de Physique*, 37(12):1445–1452, 1976.

[40] ST Milner. Polymer brushes. *Science*, 251(4996):905–914, 1991.

[41] PG De Gennes. Polymers at an interface; a simplified view. *Advances in Colloid and Interface Science*, 27(3):189–209, 1987.

[42] PrG de Gennes. Conformations of polymers attached to an interface. *Macromolecules*, 13(5):1069–1075, 1980.

[43] Rigoberto C Advincula, William J Brittain, Kenneth C Caster, and Jürgen Rühe. *Polymer brushes*. Wiley Online Library, 2004.

[44] P Mansky, Y Liu, E Huang, TP Russell, and C Hawker. Controlling polymer-surface interactions with random copolymer brushes. *Science*, 275(5305):1458–1460, 1997.

[45] Jacob Klein, Eugenia Kumacheva, Dvora Perahia, Diana Mahalu, and Sharon Warburg. Interfacial sliding of polymer-bearing surfaces. *Faraday Discuss.*, 98:173–188, 1994.

[46] A Halperin, M Tirrell, and TP Lodge. Tethered chains in polymer microstructures. In *Macromolecules: Synthesis, Order and Advanced Properties*, pages 31–71. Springer, 1992.

[47] Nobel prize for physics. `http://www.nobelprize.org/nobel_prizes/physics/laureates/1986/`. Accessed: 2013-12-22.

[48] Gerhard Meyer and Nabil M Amer. Novel optical approach to atomic force microscopy. *Applied Physics Letters*, 53(12):1045–1047, 1988.

[49] Toshio Ando, Noriyuki Kodera, Eisuke Takai, Daisuke Maruyama, Kiwamu Saito, and Akitoshi Toda. A high-speed atomic force microscope for studying biological macromolecules. *Proceedings of the National Academy of Sciences*, 98(22):12468–12472, 2001.

[50] H Richter, EA Misawa, DA Lucca, and H Lu. Modeling nonlinear behavior in a piezoelectric actuator. *Precision engineering*, 25(2):128–137, 2001.

[51] John Elie Sader. Frequency response of cantilever beams immersed in viscous fluids with applications to the atomic force microscope. *Journal of Applied Physics*, 84(1):64, 1998.

[52] Christopher P. Green, Hadi Lioe, Jason P. Cleveland, Roger Proksch, Paul Mulvaney, and John E. Sader. Normal and torsional spring constants of atomic force microscope cantilevers. *Review of Scientific Instruments*, 75(6):1988, 2004.

[53] M Allegrini, C Ascoli, P Baschieri, F Dinelli, C Frediani, A Lio, and T Mariani. Laser thermal effects on atomic force microscope cantilevers. *Ultramicroscopy*, 42:371–378, 1992.

[54] O Marti, A Ruf, M Hipp, H Bielefeldt, J Colchero, and J Mlynek. Mechanical and thermal effects of laser irradiation on force microscope cantilevers. *Ultramicroscopy*, 42:345–350, 1992.

[55] JE Jones. On the determination of molecular fields. ii. from the equation of state of a gas. *Proceedings of the Royal Society of London. Series A, Containing Papers of a Mathematical and Physical Character*, 106(738):463–477, 1924.

[56] Heinrich Hertz. Uber die berhrung fester elastischer korper. *J. fur die reine u. angew. Math.*, 92, 1882.

[57] Kenneth Langstreth Johnson and K Kenneth Langstreth Johnson. *Contact mechanics*. Cambridge university press, 1987.

[58] Olga Borozenko. Frequency response of cantilever beams immersed in viscous fluids with applications to the atomic force microscope. *Journal of Applied Physics*, 84(1):64, 2013.

[59] Uri Raviv, Suzanne Giasson, Nir Kampf, Jean-François Gohy, Robert Jérôme, and Jacob Klein. Lubrication by charged polymers. *Nature*, 425(6954):163–165, 2003.

[60] Jacob Klein, Eugenia Kumacheva, Diana Mahalu, Dvora Perahia, and Lewis J Fetters. Reduction of frictional forces between solid surfaces bearing polymer brushes. *Nature*, 370(6491):634–636, 1994.

[61] Jacob Klein. Shear, friction, and lubrication forces between polymer-bearing surfaces. *Annual review of materials science*, 26(1):581–612, 1996.

[62] Omar Azzaroni. Polymer brushes here, there, and everywhere: Recent advances in their practical applications and emerging opportunities in multiple research fields. *Journal of Polymer Science Part A: Polymer Chemistry*, 50(16):3225–3258, 2012.

[63] Hanns Fischer. The persistent radical effect: a principle for selective radical reactions and living radical polymerizations. *Chemical Reviews*, 101(12):3581–3610, 2001.

[64] Craig J Hawker, Anton W Bosman, and Eva Harth. New polymer synthesis by nitroxide mediated living radical polymerizations. *Chemical Reviews*, 101(12):3661–3688, 2001.

[65] Krzysztof Matyjaszewski and Jianhui Xia. Atom transfer radical polymerization. *Chemical Reviews*, 101(9):2921–2990, 2001.

[66] Alexei A Gridnev and Steven D Ittel. Catalytic chain transfer in free-radical polymerizations. *Chemical reviews*, 101(12):3611–3660, 2001.

[67] Rachel J Cannara, Michael Eglin, and Robert W Carpick. Lateral force calibration in atomic force microscopy: A new lateral force calibration method and general guidelines for optimization. *Review of scientific instruments*, 77(5):053701–053701, 2006.

[68] John E Sader, James WM Chon, and Paul Mulvaney. Calibration of rectangular atomic force microscope cantilevers. *Review of Scientific Instruments*, 70:3967, 1999.

[69] Christopher P Green and John E Sader. Torsional frequency response of cantilever beams immersed in viscous fluids with applications to the atomic force microscope. *Journal of applied physics*, 92(10):6262–6274, 2002.

[70] U Rabe, K Janser, and Wt Arnold. Vibrations of free and surface-coupled atomic force microscope cantilevers: theory and experiment. *Review of Scientific Instruments*, 67(9):3281–3293, 1996.

[71] FT Limpoco, Rigoberto C Advincula, and Scott S Perry. Solvent dependent friction force response of polystyrene brushes prepared by surface initiated polymerization. *Langmuir*, 23(24):12196–12201, 2007.